REPORT DOCUMENTATION PAGE

Form Approved
OMB No. 0704-0188

Public reporting burden for this collection of information is estimated to average 1 hour per response, including the time for reviewing instructions, searching existing data sources, gathering and maintaining the data needed, and completing and reviewing this collection of information. Send comments regarding this burden estimate or any other aspect of this collection of information, including suggestions for reducing this burden to Department of Defense, Washington Headquarters Services, Directorate for Information Operations and Reports (0704-0188), 1215 Jefferson Davis Highway, Suite 1204, Arlington, VA 22202-4302. Respondents should be aware that notwithstanding any other provision of law, no person shall be subject to any penalty for failing to comply with a collection of information if it does not display a currently valid OMB control number. **PLEASE DO NOT RETURN YOUR FORM TO THE ABOVE ADDRESS.**

1. REPORT DATE (DD-MM-YYYY) 01-11-1007	2. REPORT TYPE Final Technical	3. DATES COVERED (From - To) 01-01-2004 - 01-01-2007

4. TITLE AND SUBTITLE
Atmospheric Polarization Imaging

5a. CONTRACT NUMBER
FA9550-04-1-0037

5b. GRANT NUMBER

5c. PROGRAM ELEMENT NUMBER

6. AUTHOR(S)
Joseph A. Shaw

5d. PROJECT NUMBER

5e. TASK NUMBER

5f. WORK UNIT NUMBER

7. PERFORMING ORGANIZATION NAME(S) AND ADDRESS(ES)
Montana State University, Bozeman, Montana 59717

Office of Sponsored Programs
307 Montana Hall
Bozeman, MT 59717-0001

8. PERFORMING ORGANIZATION REPORT NUMBER

9. SPONSORING / MONITORING AGENCY NAME(S) AND ADDRESS(ES)
Air Force Office of
Scientific Research
875 N. Randolph St., Rm. 3112
Arlington, VA 22203

10. SPONSOR/MONITOR'S ACRONYM(S)
AFOSR

11. SPONSOR/MONITOR'S REPORT NUMBER(S)

12. DISTRIBUTION / AVAILABILITY STATEMENT

Distribution Statement A: unlimited

AFRL-SR-AR-TR-07-0492

13. SUPPLEMENTARY NOTES

14. ABSTRACT
A full-sky imaging polarimeter has been developed to measure the four Stokes parameters in each pixel of a full-sky image. The Stokes image set can be acquired in typically less than 1 sec., making possible polarimetric measurements in a partly cloudy sky without creating artifacts from moving clouds. This instrument was used to study the variation of atmospheric polarization with cloudiness, finding that the degree of polarization is consistently less in the clear portions of a partly cloudy sky than in a fully clear sky. The instrument also was applied in a validation study of the polarized MODTRAN radiative transfer code. This validation showed that the code generally performs well in conditions of low aerosol optical depth, but the single-scattering model breaks down with higher optical depths. The study shows the need for improved aerosol characterization in future polarization studies, as aerosols have a very large influence on the observed polarization state of visible skylight.

15. SUBJECT TERMS

16. SECURITY CLASSIFICATION OF:			17. LIMITATION OF ABSTRACT	18. NUMBER OF PAGES	19a. NAME OF RESPONSIBLE PERSON
a. REPORT	b. ABSTRACT	c. THIS PAGE			19b. TELEPHONE NUMBER (include area code)

Standard Form 298 (Rev. 8-98)
Prescribed by ANSI Std. Z39.18

Atmospheric Polarization Imaging – Final Technical Report
Joseph A. Shaw – Montana State University

Introduction

The use of polarization in military and environmental remote sensing has increased in recent years in continuing efforts to increase the information content of passive and actively observations. However, the polarization signature of an object depends strongly on the background light provided by the atmosphere and the natural environment. In the visible and near-infrared spectral regions, the observed polarization signatures vary significantly with cloudiness and aerosol content in the atmosphere. Attempts to model polarized radiative transfer in the atmosphere depend on accurate representations of partially polarized skylight. Therefore, efforts to exploit polarization in this spectral region requires detailed knowledge of how atmospheric polarization varies with atmospheric conditions and how that variable polarization can be represented by polarized radiative transfer models such as the polarized MODTRAN code being developed by the U.S. Air Force Research Laboratory.

In a response to the need for improved understanding and predictive capabilities regarding atmospheric polarization, we proposed an effort with the following three principal objectives:

1. Develop an all-sky imaging polarimeter capable of measuring the polarization state of skylight in an atmosphere with changing cloudiness (a critical element was to carefully determine the calibration uncertainty);
2. Apply the imaging polarimeter to studying how the polarization state of skylight depends on cloudiness;
3. Investigate how the cloud-influenced variably polarized skylight compares with model predictions from the polarized MODTRAN radiative transfer code.

This report summarizes the accomplishments in these three areas. The following sections describe the full-sky imaging polarimeter system developed in this project, show examples of data obtained with this instrument, and discuss the results of comparing measurements with models.

All-Sky Imaging Polarimeter System

A very significant result of this study was the development, calibration, and validation of an imaging polarimeter that can measure the four Stokes parameters in each pixel of an all-sky image in five 10-nm-wide spectral bands centered at 450 nm, 490 nm, 530 nm, 630 nm, and 700 nm. An added feature of this instrument is that it has been designed with front-end optics modules that can be swapped out to convert the polarimeter from its all-sky "fisheye" mode to a telephoto mode that is useful for measuring polarization signatures of small or distant objects.

Several types of full-sky polarimeters have been built previously, but none was suited to measuring skylight polarization in variably cloudy conditions. Appreciable cloud motion during the image-acquisition cycle generates polarization artifacts (Pust and Shaw 2006; Tyo et al. 2006), so the key feature needed in this study was the ability to

acquire a full set of Stokes polarization images faster than approximately 1 second. Furthermore, digital image acquisition was deemed necessary to avoid the inevitable calibration uncertainties and time delays inherent in film processing. Previous full-sky imaging polarimeters have either relied on film processing (Horvath et al. 2002; North and Duggin 1997), with its inevitable calibration uncertainties and long time delays, or have made use of electronic imaging in a configuration that prohibited imaging of cloudy skies because of long image-acquisition times (Voss and Liu 1997; Liu and Voss 1997).

<u>System Design</u>

The system we developed builds on the strengths of the Voss-Liu system while minimizing the total measurement time to allow studying more highly variable sky conditions. This system also has front-end optics modules that can be quickly changed from a fisheye to a telephoto format to observe narrow fields of view. Rather than using rotating polarization elements to generate Stokes images at each spectral band, this instrument relies on liquid crystal variable retarders (LCVRs) to electronically vary the polarization state of the light incident on a single CCD camera. This typically allows full Stokes images to be obtained in less than 0.5 s in each spectral channel (we still use a rotating filter wheel to change the spectral band). The design of the instrument focused on four goals: 1) provide easily changeable optics to allow alternate views of narrow and full-sky fields of view; 2) keep incident angles on the polarization optics small to minimize problems caused by the incidence-angle-dependent LCVR variable retardance; 3) optimize aberrations to provide image spot sizes smaller than or comparable to the pixel size; 4) minimize acquisition time over each measurement.

In the system design, a polarimetric accuracy of 1% was desired. Eight-bit data, with its 0.39% quantization error, could potentially cause polarization errors of ~1% with system matrix condition numbers of ~2, so to eliminate this error, only cameras incorporating better than 8-bit data where considered. To meet the requirements of fast image acquisition, a DALSA 1M30 camera was chosen. This 1-Mpixel camera exhibits 12-bit data, frame speeds up to 30 frames per second and download times that are much shorter than the exposure time. Large 13-um pixels simplified aberration optimization.

Two lenses were selected for the front-end, a Nikon 300 mm telephoto lens and a Nikon 16 mm fisheye lens. Since these lenses are designed to form a 35 mm film image (24 x 36 mm), the image needed to be reduced to fill the 13 mm CCD chip with the full fisheye field of view. Each front lens—the telephoto and fisheye—was focused onto a field lens at the image plane. This image was reimaged by a Micro-Nikkor 105 mm lens to the size of the 13-mm CCD chip. The selection of the 105 mm micro lens also reduced the maximum ray incidence angle to less than 5°. The field lens was chosen to eliminate vignetting on the 105-mm micro lens. Spectral filters of 10 nm wavelength centered at 450, 490, 530, 630, and 700 nm currently are used in the system. Figure 1 shows the ZEMAX layouts with the telephoto and fisheye front-end lenses (lens prescriptions were obtained from Nikon patents). Figure 2 is a photograph of the polarimeter back end, containing the polarization and re-imaging optics. Figure 3 is a photograph of the system operating in zenith-viewing full-sky mode (the blue foam pieces are insulating the LCVRs).
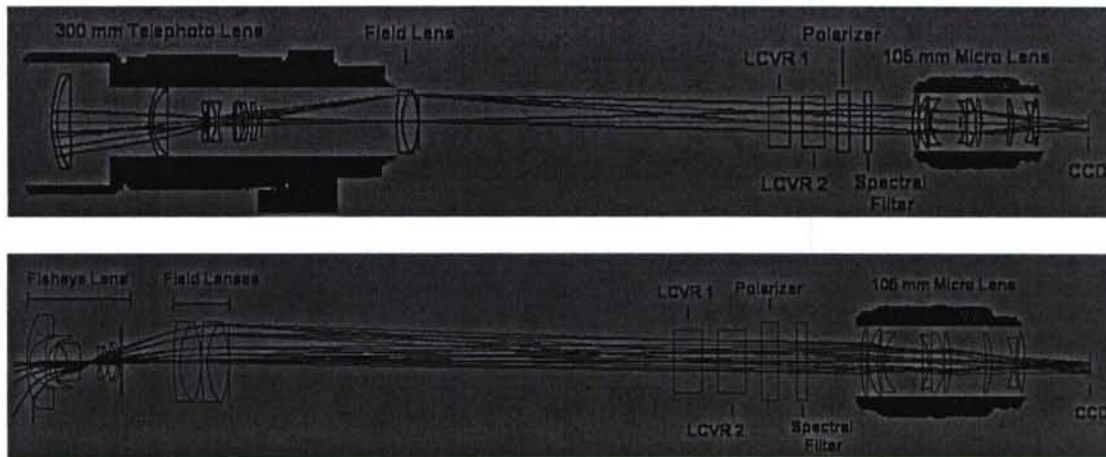
Figure 1. Imaging polarimeter designs with the telephoto (top) and fisheye (bottom) front-end optics. Lens casings are shown for reference. Since the telephoto system is longer, the scale is not the same for each system version.
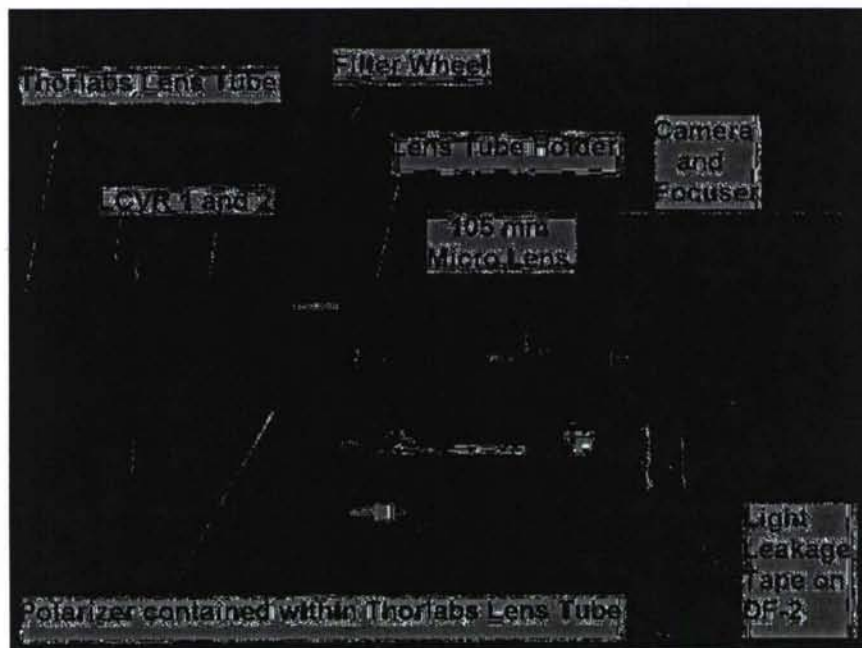

Figure 2. Back section of the polarimetric imager.

Two Meadowlark LRC-300 temperature-controlled LCVRs were used in the system, along with a fixed linear polarizer, to change the instrument polarization state. Any effects of polarization-dependent response of the detector and optics behind the polarizer are removed since only one polarization state is seen beyond the polarizer. The

retarders have been measured to completely change retardance in 55 ms (without the special TNE waveform, which can speed it up by approximately a factor of two). Time of measurement over the four images varies between 0.3 and 1.2 seconds (dependent upon exposure time), although further optimization using the TNE could reduce the time further. Errors resulting from changing skies are negligible at this acquisition speed.
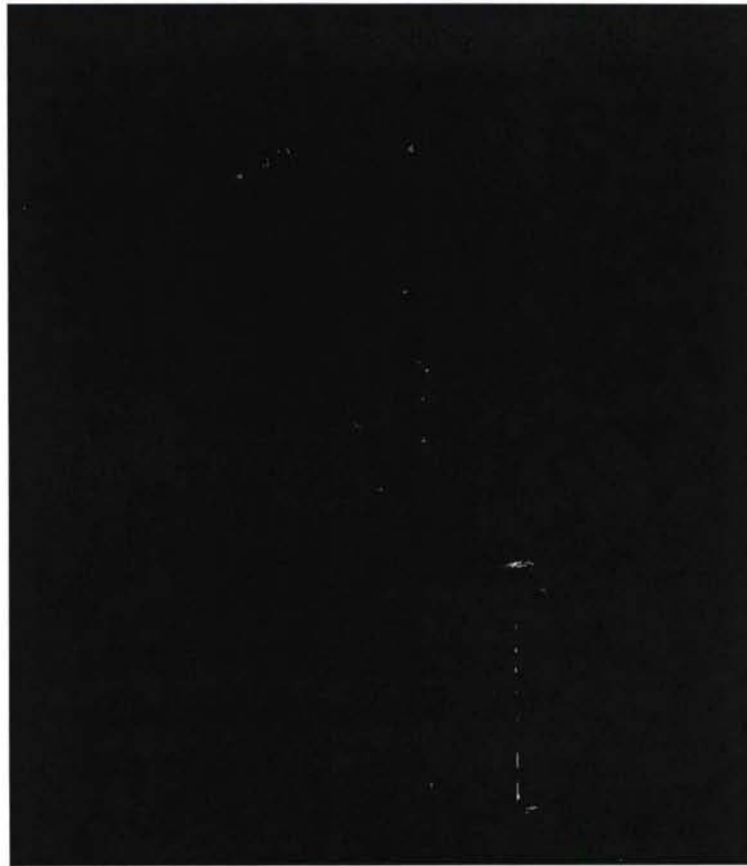

Figure 3. The imaging polarimeter designed in this project, shown in full-sky mode.

The overall objective of a Stokes polarimeter is to determine S, the Stokes vector of input light, from successive power measurements made with different instrument polarization states. We selected LCVR fast-axis angles and retardances to achieve an optimal system matrix, then calibrated the instrument to determine the values of the system matrix elements corresponding to these settings (Pust 2007; Pust and Shaw 2006; Tyo et al. 2006). Measurements from the resulting instrument are multiplied by the system matrix inverse to recover the input Stokes vector of each pixel in the scene.

The LCVR retardances are tuned electronically to change the polarization state of the instrument. To reduce the amplification of image-exposure errors to Stokes-vector errors during Stokes vector retrieval, the retardances of the LCVRs for each image should

be chosen to minimize the condition number of the system matrix (Tyo 2002; Tyo 2000; Sabatke et al. 2000). Condition number relates how the error is propagated; for example, if the condition number of A is 2, and the error in the exposure is 1%, the error in the Stokes parameter is expected to be 2%.Optimization for this instrument followed the work of Tyo (2002). The MATLAB (ver. 7.0.4) Optimization Toolbox (3.0.2) was used to optimize the fixed fast-axis orientation angle (with respect to the fixed linear polarizer axis) and the set of four retardances for each LCVR, with the LCVRs modeled as perfect retarders. This generates ten variables that are optimized to yield a minimum value of the system matrix condition number. Retardance values were constrained from 0 to 180° (half-wave retardance)—although this is not strictly necessary. Many different sets of rotation angles and retardance angles with equivalent condition numbers could be found by varying initial conditions; the set we chose to implement is shown in Table 1.

Table 1. Retarder settings for two-LCVR polarimeter.

	Retarder1	Retarder2
Fast-axis fixed rotation angle	115.0°	45.0°
Retardance Angles		
Image 1 (polarimeter state 1)	150.5°	105.2°
Image 2 (polarimeter state 2)	27.7°	180.0°
Image 3 (polarimeter state 3)	180.0°	15.4°
Image 4 (polarimeter state 4)	18.17°	64.77°
Condition Number (2 norm)	1.82	

Because the retardance and equivalent rotation angles for LCVRs have been shown to change according to incidence angle (Xiao et al. 2003), the system must be designed and calibrated carefully to account for this. For instance, every pixel must be calibrated separately at each F/#, and the focus cannot be varied without altering the calibration (Pust 2007; Pust and Shaw 2006).

<u>System Calibration</u>
For each image, dark current is removed by subtracting a stored dark image at an exposure of 50 ms. Because longer exposures slightly increase the dark current, an exposure-dependent uniform correction is also subtracted from the image. Linearity tests of the camera using an integrating-sphere uniform-luminance standard showed that the linearity rolls off slightly in the top half of the dynamic range, producing a 4% radiance error at the top. To remove this effect, a correction equation is used to correct each pixel.

For each pixel, wavelength, and f/#, calibration was needed to find the actual values of the system matrix, A. The first three values of each row of the system matrix can be found by use of a linear polarizer. Images were taken with a large-aperture linear polarizer (extinction ratio better than 10^{-3}) oriented at −90°, 0°, -45°, and 45° for each polarimeter state with the instrument looking into a 10-cm-aperture luminance standard. This corresponds to the normalized Stokes vectors, [1 1 0 0], [1 −1 0 0], [1 0 1 0], and [1

0 -1 0]. The image values measured at each of these settings were used to determine the first three components of the row. Each of the other three rows was measured in a similar fashion. The last column of the system matrix could not be measured using only a linear polarizer (a large-aperture achromatic waveplate was not available for our work), so the last column of the system matrix was modeled according to the retardances and equivalent rotation angle of each LCVR, assuming pure retarders. This measurement of the first three columns of the system matrix and the modeling of the last column was done for every pixel and every spectral filter at four different f/#s (2.8, 4.0, 5.6, and 8).

Four different polarizer positions—22.5°,-67.5°, –22.5°, and 67.5°—were used to validate the calibration. These states were chosen because they were different than the calibration settings. Unpolarized light was also measured. Finally, circular polarization was created using a 2.5-cm achromatic waveplate. There is uncertainty in the exact Stokes vector obtained with the achromatic waveplate, as the retardance is dependent upon the incidence angle of light and the wavelength, and the exact position of the fast axis changes with wavelength. Nevertheless, an estimate for the accuracy of the fourth column model could be found by measuring light from the achromatic waveplate. Table 2 shows the maximum errors recorded through all four f/#s.

Table 2. Summary of maximum errors without front lenses.

Error	Linear Input (100 %)	Unpolarized Input	Circular Input
S_1 and S_2	+/-1.1%	+/-0.4%	unknown
S_3	+/-1.5%	+/-0.3%	-10%

The model of the last column of the system matrix seems to cause under-estimation of the magnitude of the circular Stokes parameter at 90%. Even with the uncertainties in the achromatic waveplate, higher values of the circular component were expected. For all foreseeable measurements, the light will be partially polarized linear light. If circular light is found, the instrument will measure a circular signature, but not necessarily with high quantitative accuracy until we complete the circular polarization calibration with a large-aperture achromatic waveplate. This is acceptable, since circular polarization is not expected to be found in either sky or targets. The overall linear polarization accuracies seem to be limited by slight exposure jitter in the camera.

The front lenses, which also alter the Stokes parameters of incident light, were calibrated separately from the polarimeter, though it would also be possible to calibrate the entire system together with each lens. Since lenses exhibit very little depolarization (Chipman 2005) and their Mueller matrices are well conditioned, the Mueller matrix of the front lens can be inverted and multiplied by the measured Stokes vector to obtain the input Stokes vector. Calibration of the lenses followed a method that is similar to the system matrix calibration. A Stokes vector is measured with a linear polarizer at -90°, 0°, -45°, and 45°. Using the measured output Stokes vectors and the known input Stokes vectors, the first three columns of the lens Mueller matrix were found. The matrix was assumed to be a symmetric, non-depolarizing Mueller matrix and the last column calculated.

Calibration of the fisheye lens was accomplished with piecewise measurements across the field of view of the instrument. The luminance standard and polarizer were rotated in a plane defined by the optical axis and the polarizer orientation in the image. This arrangement only calibrated a slice across the center of the fisheye image. To calibrate the whole image, the polarimeter was rotated -45°, 45°, 0°, and 90° to obtain slices that covered the whole image area.

One problem with the fisheye calibration is the issue of reference plane. The fisheye itself rotates the polarization vector. As an example, consider a fisheye lens viewing the sky dome with the horizon at 90° from the optical axis (because the imager is looking up). The orientation of the polarizer sets the zero–azimuth angle. Horizontal polarization is parallel to the horizon. Light incident from the horizon at 0° azimuth with a *vertical* polarization vector will be measured to have an angle of polarization of 0° by the polarimeter; however, light incident from the horizon at 90° of azimuth with *horizontal* polarization also will be measured to have an angle of polarization of 0°. Finally, a field incident upon the fisheye from the horizon at 45° of azimuth with a 45° polarization vector will also be measured to have a polarization angle of 0°. Should an incident ray from the horizon that has polarization parallel to the horizon always be measured as the same polarization angle? This is a matter of choice. If all horizontally polarized light at the horizon is measured to have the same polarization angle, there will be a discontinuity at the center. If the rotation of the fisheye is maintained, there will not be a discontinuity, but interpreting angle-of-polarization data is more challenging. Even with this challenge, the latter method was chosen to avoid an additional rotation in the fisheye lens calibration matrix. Post-processing algorithms could be used to convert between the two types of referencing (i.e., change between horizon reference and instrument-polarizer reference).

Because the fisheye rotated the polarization vector, the calibration polarizer images have a polarization angle that varies across its aperture. Therefore, for each piecewise slice, the only accurate angle of polarization was at a line across the center of the slice. For each of the slices, a line was extracted across the accurate part of the calibration slice. Calibration data were then linearly interpolated between each of these calibration lines. In the center of the image all the slices converged upon the same calibration so the center was calibrated in a block without interpolation. The accuracy of the interpolation was of concern, but validation experiments shows that the calibration worked well. After calibration of the telephoto lens, validation was performed identically to the system matrix validation using 22.5°,-22.5°, 67.5°, and -67.5° polarizer angles. None of the errors in circularly polarized, linearly polarized, or unpolarized light changed significantly. Expected Stokes-vector reconstruction error in the telephoto lens is less than ±1.5%.

Fisheye validation used the same method, but multiple validation images were taken across the field of view. For images that were in the interpolated areas, it was difficult to know the exact angle of polarization as it changed across the image of the luminance standard. Nevertheless, the angle of polarization did not seem to depart from what was expected in the center of each image. Errors in the degree of polarization were

±1.5%, with worst errors of up to -4% in the area within 40 pixels of the center. Circular errors were significantly worse (±5%), probably because the circular polarizer models were not entirely valid. (As mentioned before, this is not a huge problem since circular polarization is not expected in the sky.) Angle-of-polarization error in the center of the fisheye image was ±0.3°. The condition number for the whole imager varied from 1.85 to 2.3 across all f/#s, wavelengths, and pixels. Depolarization in the LCVRs does not seem to significantly reduce the conditioning of the system matrix.

As mentioned previously, the calibration was not expected to remain valid if the f/# of the system was changed. Therefore, to verify this idea, we made measurements at f/2.8, f/4.0, f/5.6 and f/8.0, using the calibration for the f/4.0 setting. Table 3 shows the average degree of polarization for fisheye measurements obtained with the instrument viewing a linear polarizer oriented at -67.5°. There is clearly a rise in the degree of polarization determined with the f/4 calibration as the imager is stopped down. This is expected because setting the instrument at a larger aperture creates more depolarization in the LCVRs. For a set calibration, the lower f/#s should measure a lower polarization. This confirms the conclusion that each f/# should be calibrated separately, although in this imager it does not seem to be an excessively large problem. The low incidence angles (<5°) probably minimize the problems of depolarization in the LCVRs.

Table 3. Measured degree of polarization (DOP) using the f/4.0 Calibration

f/#	Measured DOP
F2.8	100.10%
F4.0	100.80%
F5.6	101.33%
F8.0	101.32%

Full-Sky Polarization Measurements

The primary variables affecting the Degree of Linear Polarization (DoLP) of skylight are solar elevation (or zenith) angle, clouds, and aerosols. Each of these variables can reduce the DoLP from the expected signature of a Rayleigh-scattering atmosphere.

The Effects of Varying Solar Zenith Angle

A Rayleigh-scattering atmosphere generates a band of highly polarized light that stretches across the sky, 90° from the Sun. The expected peak amplitude of skylight polarization varies with wavelength, solar zenith angle, and atmospheric conditions (Coulson 1988; Pust and Shaw 2006; Pust 2007). In our study, whenever we must compare data from multiple days, we only compare data taken at the same solar elevation angle to avoid airmass variations to influence the apparent results. Figure 4 shows a time-series plot of the maximum DoLP measured with our full-sky polarimeter throughout a clear-sky afternoon. The DoLP rises to larger amplitude as the sun sets. This figure and others like it in this report are adapted from Pust (2007), a Ph.D. dissertation prepared from work conducted with AFOSR support in this project. Each line has a color that corresponds approximately to the wavelength of the polarimeter channel, except black that represents the invisible 700-nm band.
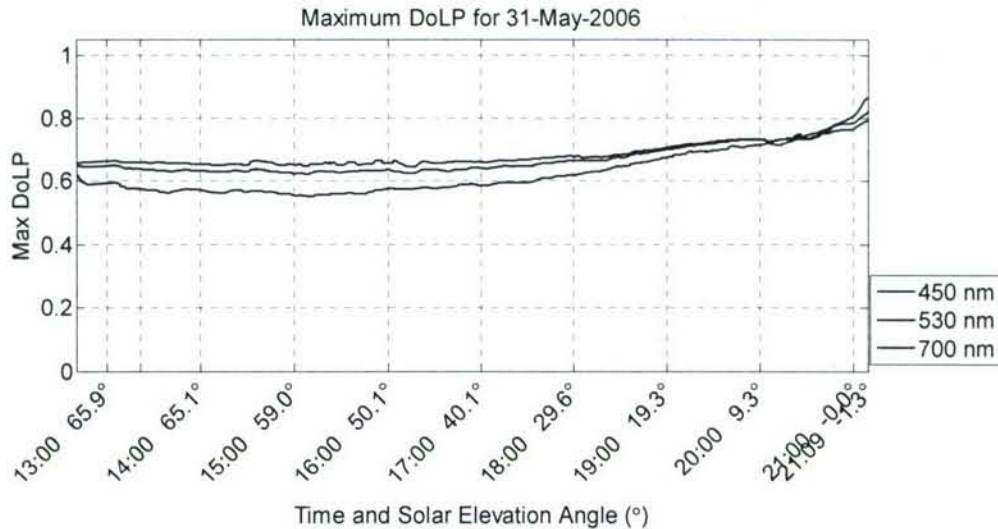
Figure 4. Effect of solar elevation angle on DoLP. The colors used to plot the wavelengths represent their actual color as perceived by a human observer. 700 nm is plotted as black since it is not visible to the human eye.

Although longer column length is one process that adds to multiple scattering, Coulson has shown that reduction of the DoLP at high solar elevation angles is exacerbated by the column illumination by molecules on the horizon below the region of maximum degree of polarization (Coulson, 1988). During mid-day the molecules on the horizon below the area of maximum degree of polarization are directly illuminated, so they contribute more to this multiple scattering. As the sun moves lower, these molecules become engulfed in the Earth's shadow, so they no longer contribute to the multiple scattering. Surface reflection from the horizon also is eliminated, so multiple scattering is at a minimum around sunrise and sunset. Therefore, at sunrise and sunset, the maximum degree of polarization is closer to the higher single-scatter approximation.

Still, a portion of the reduction in DoLP during the mid-day is caused by the increase in optical depth of the column. We investigated the use of an airmass correction to the polarimeter signal, similar to what is done with solar radiometer data, but found that this is inadequate. Correcting the DoLP for the airmass is not as simple as correcting solar radiometer data for airmass because the optical depth depends only on the multiple scattering in and out of the direct path, while the DoLP is dependent upon the multiple scattering in the observing path and the illuminating path. Therefore, using an airmass correction does not provide any significant benefit compared to using the original data.

Aerosol Effects
The DoLP is very sensitive to the aerosol content of the atmosphere. These scatterers significantly reduce the DoLP. Figure 5 shows data for three days with widely varying optical depths. The aerosol optical depth (AOD) values at a wavelength of 500 nm for September 25, 2006, September 11, 2006, and September 5, 2006 were roughly 0.05, 0.10, and 1.05, respectively.

The separation of 700 nm from the group for September 5, 2006 demonstrates the wavelength dependence of the effects of aerosols. Although aerosols tend to affect all wavelengths similarly, there is a wavelength dependence of the magnitude of DoLP reduction. This reduction appears to depend on aerosol type and size distribution. Also, notice that when compared to sunset data, the mid-day 700-nm DoLP remained higher than the other wavelengths, yet for lower optical depths it always moved lower during the mid-day. The cause of this difference may be unrelated. For the low aerosol days, the drop of the 700-nm DoLP below that at shorter wavelengths is attributed to the fact that Rayleigh scattered light falls off with wavelength. For any wavelength, the polarization measured is a merger of the highly polarized light from the upper atmosphere and the lower polarized light from Mie scattering in the aerosol-laden boundary layer. Since very little light is Rayleigh scattered at 700 nm, the increase of the observed optical depth, especially in the boundary layer, as the sun moves higher in the sky causes the 700-nm DoLP to be more affected by the aerosols than the DoLP at shorter wavelengths. For high aerosol days, the polarization signature is dominated by both single and multiple aerosol scattering in the boundary layer. Polarization effects are highly dependent upon the Mie scattering phase function of the aerosol type and size distribution. Therefore, the fact that the 700-nm DoLP is higher in this case could possibly be a chance property of the forest fire aerosols present. For other aerosols, the 700-nm DoLP could possibly be lower than at shorter wavelengths.

Also, notice that as the optical depth approaches zero, the degree of polarization does not approach 100%. Multiple scattering of the molecular column reduces the DoLP even for an aerosol-free sky. Previous investigators have taken readings of the DoLP for the cleanest skies in the world, such as at Mauna Loa, Hawaii. Several papers show that the maximum degree of polarization measured at 700 nm never exceeds about 87% at 3° solar elevation in these clean skies (Coulson, 1988). In fact, multiple scattering, molecular asymmetries, and the random distribution of particles will cap the DoLP at ~94% for the cleanest atmosphere (Bohren, 1996). Our data taken during the clearest days of September 25 and May 31, 2006 found maximum degree of polarization values of about 88% at 700 nm for 3° solar elevation. Considering that the instrument has an error estimate of ±3%, the data taken in Bozeman is not unreasonable--although it does seem impressive that Bozeman occasionally reaches the level of purity found at Mauna Loa. (For this instrument, data beyond about -2° of solar elevation is too noisy to be trusted. To create a buffer, 3° was taken as the minimum reliable solar elevation for a clear sky.) To obtain reliable data at lower solar elevation angles, much wider bandpass filters are necessary to provide a stronger signal on the detector.
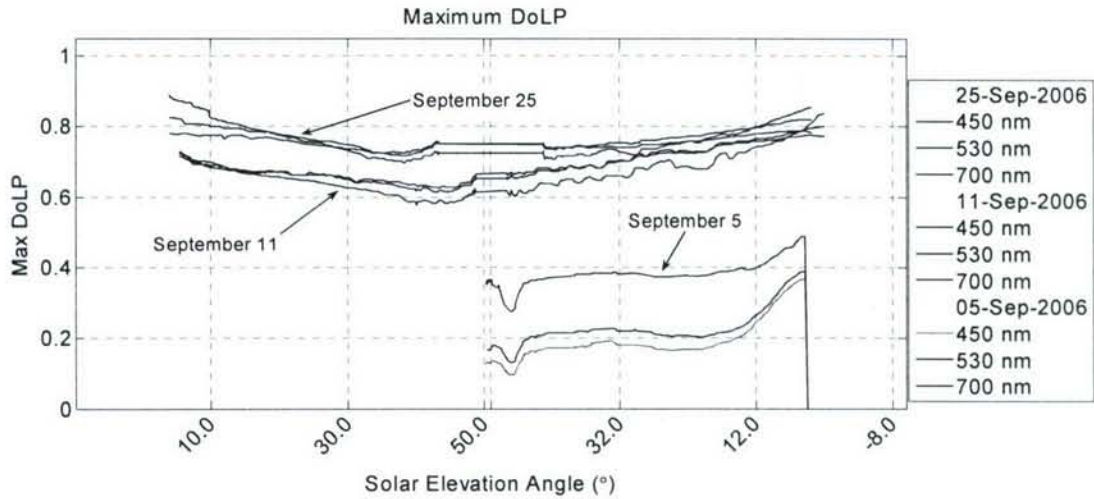
Figure 5. Effect of aerosols on DoLP.

Cloud Effects on Polarization

Strong multiple scattering causes clouds to severely reduce the degree of polarization observed when looking at the cloud. Figure 6 is a full-sky polarization image measured with our instrument. This is a 450-nm image of DoLP for the full sky dome, with blue representing zero and red 100% polarization. The cloudy pixels are clearly very significantly reduced in DoLP relative to the neighboring clear pixels, and in fact approaches zero. In fact, when looking at a thick cloud, typically the only measurable DoLP is from the Rayleigh scattered light between the observer and the cloud.
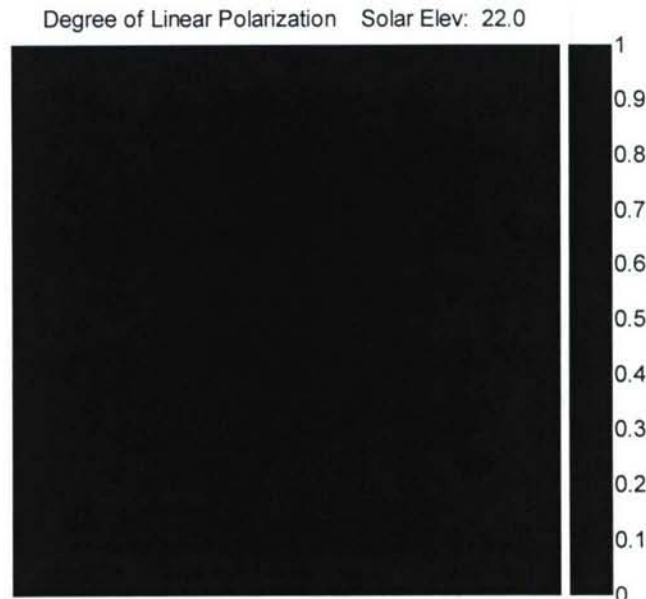
Figure 6. Example of cloud effects on DoLP at 450 nm. The clouds appear as largely unpolarized sources that reduce the otherwise relatively highly polarized skylight.

Because the polarized MODTRAN-P radiative transfer code is a single-point code, it does not model anything outside of the scattering geometry of the simulated atmospheric column. The effects of clouds (or clear sky) in other areas of the sky upon the observed column are totally ignored in the model. This generates two important questions concerning the viability of modeling atmospheric polarization with a single-point code such as MODTRAN: (1) Do clouds affect the polarization in clear portions of a partly cloudy sky? (2) How much will the polarization measured looking at one cloud be affected by the presence of clouds elsewhere? If either of these issues is significant, then MODTRAN-P or its applications may need to be modified.

Overcast-Sky Polarization

For all overcast skies that have clouds thick enough to not directly transmit the skylight above the cloud, the DoLP is zero within the error margin of the instrument. Figure 6 shows an overcast sky on April 11, 2006 at 18:00 MDT at 700 nm. Notice that, with the exception of some slight (<2%) DoLP that is generated by errors in the fisheye lens Mueller matrix, the DoLP of the entire sky is zero. The buildings on the top and right of the image appear slightly polarized, presumably through reflection. The clouds act as a uniform source from all directions, thereby eliminating any observable polarization from Rayleigh scattering. This is consistent for all wavelengths.
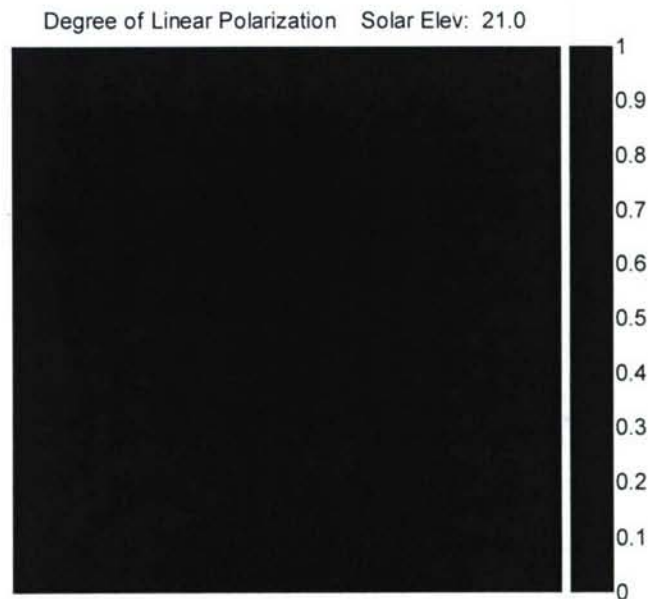
Figure 7. The DoLP for an overcast sky showing lack of skylight polarization.

Partially Cloudy Sky Polarization

For skies that are only partly cloudy, the measured polarization is dependent on both the thickness of the cloud and whether or not the column below the cloud is illuminated directly by the sun. If the cloud is thin, polarized light from scattering above

the cloud is seen by the instrument. If the column below the cloud is not illuminated directly by the sun, the illumination of the column from other clouds and the sky will reduce the DoLP beneath the cloud. Significant DoLP can only be generated by illuminating the column primarily from one direction. For an overcast sky with optically thick clouds, the most extreme scenario of zero DoLP occurs. The question of greatest interest is: for a thick cloud surrounded by clear sky, how much polarization is generated below the cloud? To answer this question, we found images containing clouds that had zero DoLP at 700 nm ("thick" clouds) and analyzed the corresponding 450-nm images.

Figure 8 shows a cloud in the band of maximum polarization, with effectively zero DoLP at the cloud. In this case, the 450-nm DoLP was as high as 4% in the same cloudy areas, as shown in Figure 9. Other examples were analyzed to study the variation of DoLP with cloud brightness (bright clouds reduce the DoLP more than dark clouds). Several cloud pictures were inspected to find clouds with the highest DoLP. Using telephoto lens data from October 20, 2005, Figures 10 and 11 show some large DoLPs that were found in cloudy pixels at 450 nm.
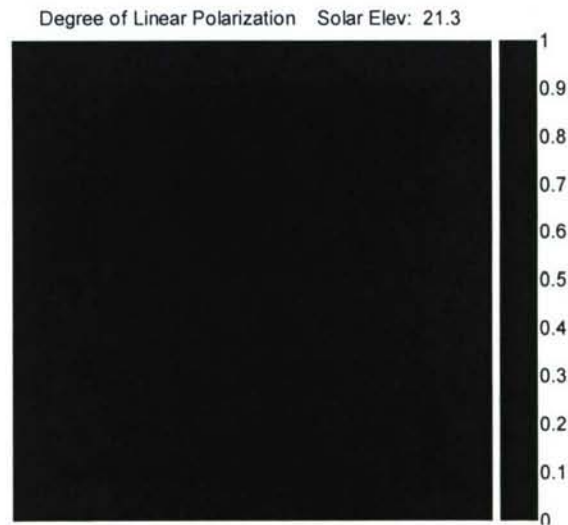
Figure 8. 700-nm DoLP for a partly cloudy sky, April 27, 2006 18:17 MDT.
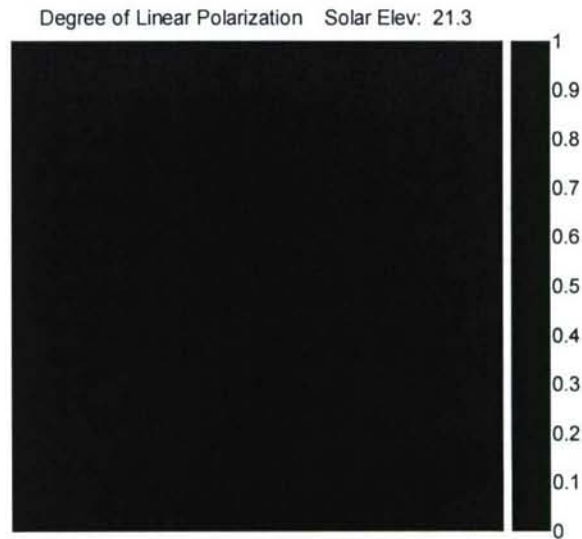
Figure 9. 450-nm DoLP for a partly-cloudy sky on April 27, 2006, 18:17 MDT.

For the images shown in Figs. 10 and 11 clouds fill the entire image. In reality, the entire sky was partially cloudy. For these low solar elevation angles, the sun directly illuminated the column underneath the cloud. In the 450-nm image, the area of the thick cloud is not physically in the same place as the 700-nm image owing to the ~25 seconds between the two images. Although this DoLP may not be considered to be an absolute maximum for the amount of DoLP generated underneath a cloud, it does show that significant DoLPs of at least 15% are possible.

Using the minimum polarization in each image finds the spots with the thickest clouds. Since many images are taken successively, the minimum in each 700-nm image will be in either the 450-nm image that precedes or follows it. Therefore, a plot of successive minimum DoLP measurements for all three wavelengths shows the amount of polarization that can be generated underneath a thick cloud (Figure 12). Thick clouds have near-zero 700-nm polarization.

Degree of Linear Polarization 700 nm   Solar Elev: 12.1
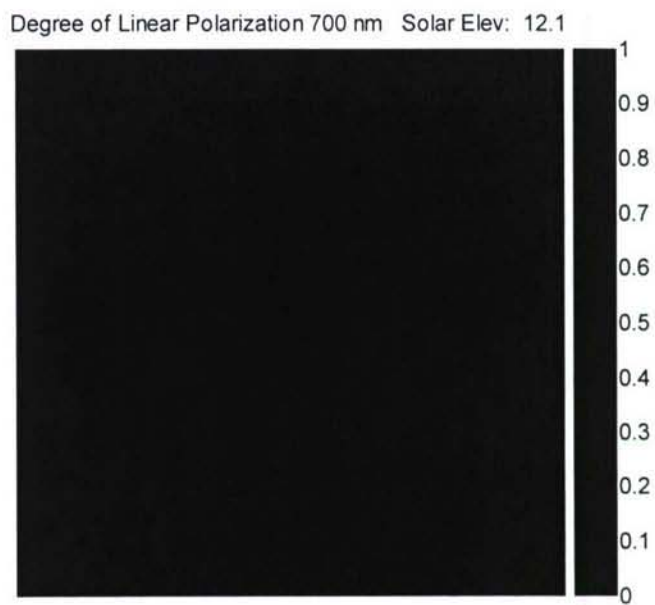
Figure 10. 700-nm DoLP for a thick cloud observed with the telephoto lens on October 20, 2005. The areas of red on the left side of the 700-nm data show an area of over exposure.

Degree of Linear Polarization 450 nm   Solar Elev: 12.0
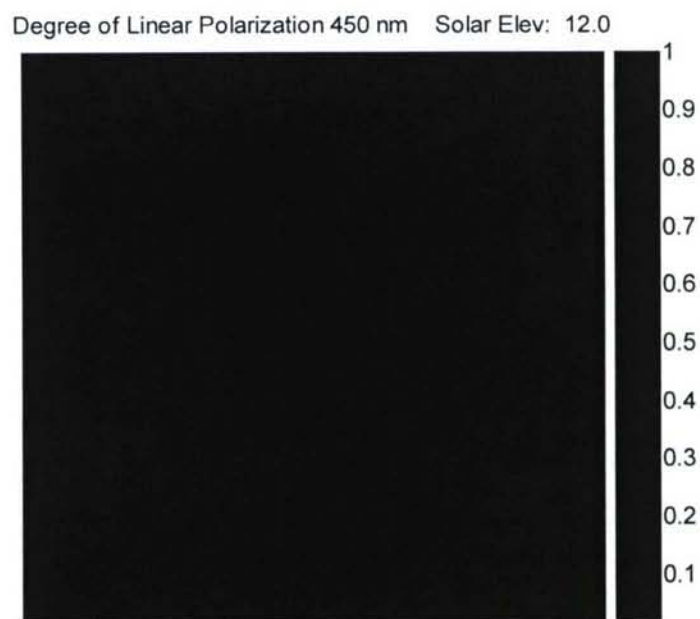
Figure 11. 450-nm DoLP for a thick cloud observed with the telephoto lens on October 20, 2005.

Minimum DoLP at Zenith for 20-Oct-2005
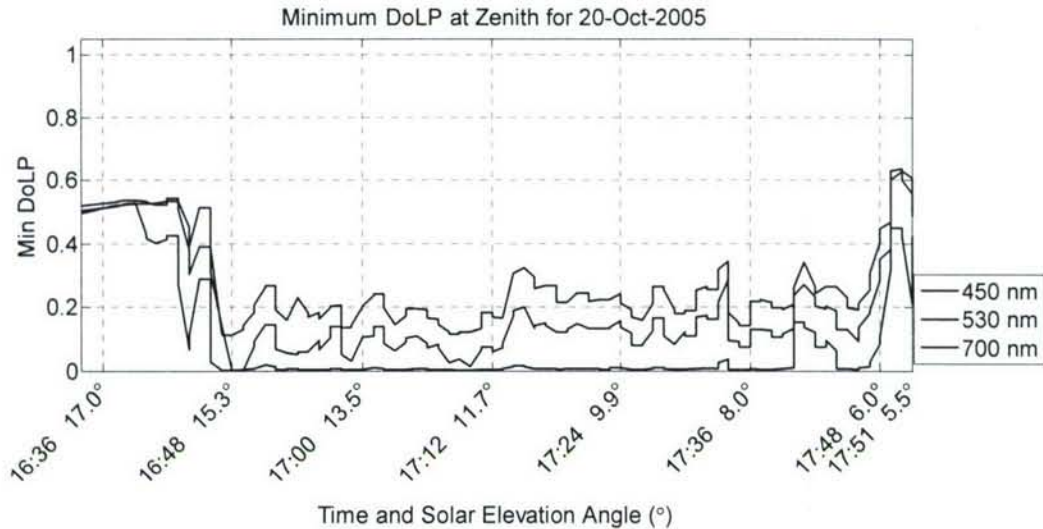
Figure 12. Minimum DoLP at zenith using the telephoto lens on October 20, 2005.

When only the areas where the 700-nm DoLP is near zero are considered, the DoLP at 450 nm is as high as 23%. DoLPs at 450 nm of this magnitude for thick clouds were never reproduced in any subsequent data—although this was the only set that used the telephoto lens. Most DoLPs generated under thick clouds measured by the fisheye lens were near 5-6% at 450 nm. The wider field of view of the fisheye does reduce the resolution to a point where the thickest cloud areas may not be seen. Local shadowing of the areas under the clouds can cause small parts of the cloud bottom to be dark and thus have a higher DoLP. Some of these areas could be missed by a combination of the lower resolution of the fisheye and the 9x9 median filtering used to reduce noise in the minimum DoLP. Without reasonable explanation for the irregularity, it is determined that the 450-nm DoLP generated under clouds can rarely reach upwards of 22%.

Effects of Clouds on Surrounding Clear Sky

It is clear from the above section that the partially cloudy skies have different DoLPs than skies that are completely overcast, but what about the opposite problem? Specifically, **do clouds reduce the degree of polarization in clear-sky portions between the clouds? And, how much do clouds affect the degree of polarization in the clear-sky portions of a partly cloudy sky?**

Because of its full-sky capability and short acquisition time, the polarimeter built for this project is uniquely suited to study this problem. Previous investigators were confined to either single-pixel measurements of the sky or full-sky images of only clear skies. This instrument can measure skies with moving clouds at full-sky resolution. Our full-sky polarization images consistently have shown that the degree of polarization is severely reduced in the areas of the sky between the clouds. Examples of this are shown in Figures 13 and 14. The large cloud on the left of the June 23 image is over the Bridger mountain range, while the small scattered clouds to the right are forming over the Gallatin mountain range. In both images, it is clear that the maximum degree of

polarization is much lower in the clear center area when clouds are present (left image) than when clouds are not present (right image). Also, this example illustrates a feature that is common to all the partially cloudy data: the 700-nm DoLP is reduced more severely than the 450-nm DoLP. From the data we have available, the aerosol content of the atmosphere seems very similar on both days. Future investigations, however, will benefit from advanced instrumentation, including a scanning solar radiometer, to characterize the aerosols in the atmosphere.

The case for the changing DoLP in Figures 13 and 14 NOT being caused simply by changes in the atmospheric aerosol content is shown in Figures 15-17. These are time-series plots of the maximum DoLP found in full-sky images at 450, 530, and 700 nm wavelengths, respectively, on three days (June 23, June 26, and Sep. 11, 2006). The key comparison is between June 23 and June 26 (the dates of Figures 13 and 14), but September 11 is shown for comparison to June 26. Although the optical depth in the afternoon is dropping—causing the maximum DoLP to be slightly lower—both the morning and evening of September 11 compare well to June 26. The difference between these days gives a reference to how well two clear skies with similar optical depths will track each other.

Degree of Linear Polarization   Solar Elev: 45.9   Degree of Linear Polarization   Solar Elev: 45.9
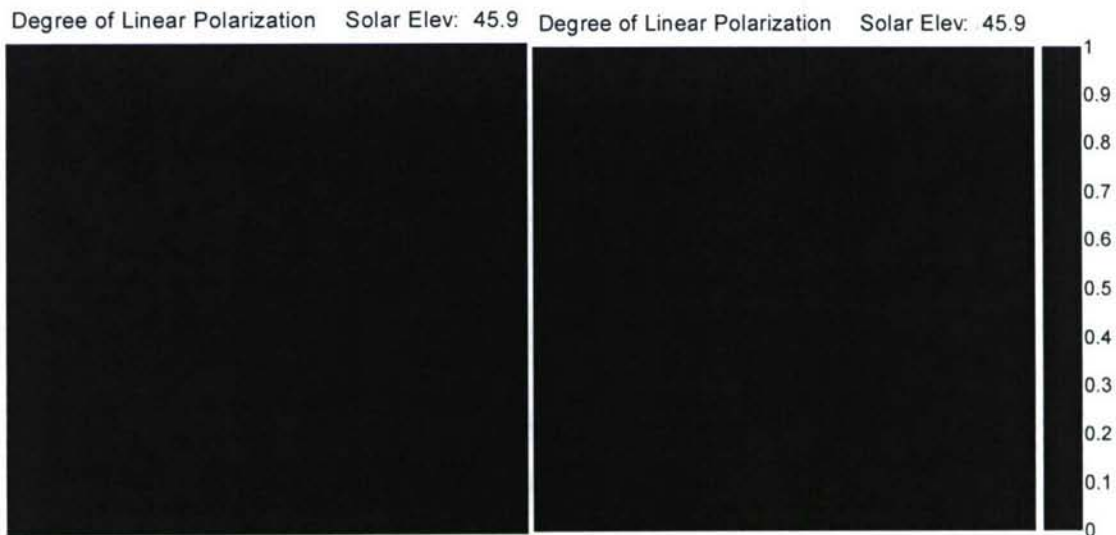
Figure 13. Comparison of a partly cloudy sky on June 23, 2006 (left) at 16:36 MDT and a clear sky on June 26, 2006 (right) at 16:36 MDT (450 nm). Areas in red are overexposed.

June 23 has some special features. First, it has a clear-sky region for most of the morning that compares well to both June 26 and September 11, 2006. At some point near the time of maximum solar elevation (65.7°), the maximum DoLP begins to drop quickly. Then, around 41° solar elevation angle (16:30), large clouds move into the sky and cause a large drop in the maximum DoLP. This is most pronounced for the 700-nm wavelength (Figure 17)—as was seen in Figures 14 and 15. Finally, after the majority of clouds clear

the sky at 31° solar elevation angle (18:00), the maximum DoLP increases but remains significantly lower than both September 11 and June 26. From 31° to 16° (18:00 to 19:27), the sky is clear in most images, but a few small clouds are seen sporadically. Since aerosols are an unlikely cause, the reduction of the maximum DoLP during the late afternoon of June 23 is likely caused by something other than aerosols.
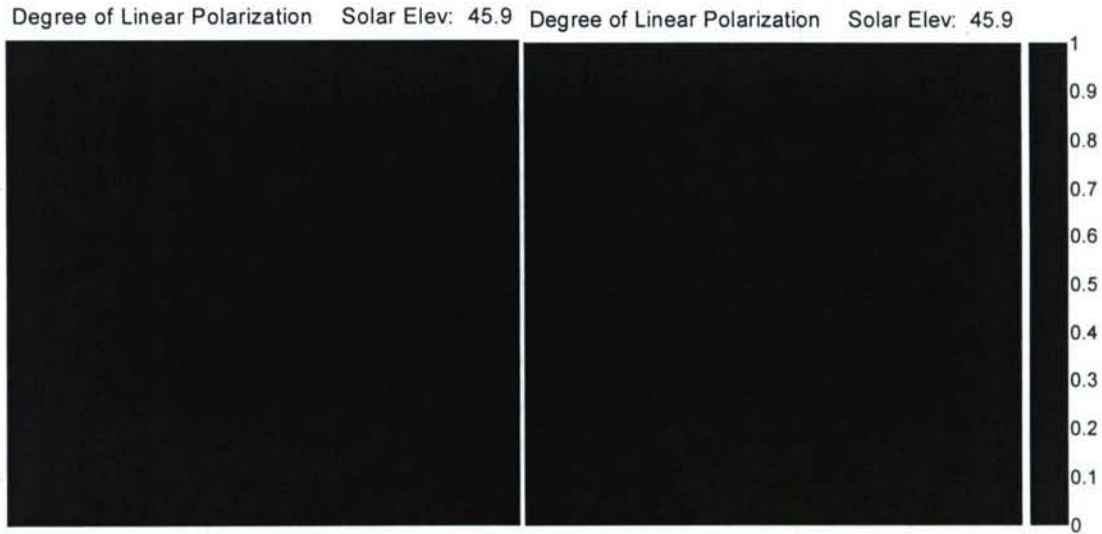

Figure 14. Comparison of a partly cloudy sky on June 23, 2006 and a clear sky on June 26, 2006 (700 nm).
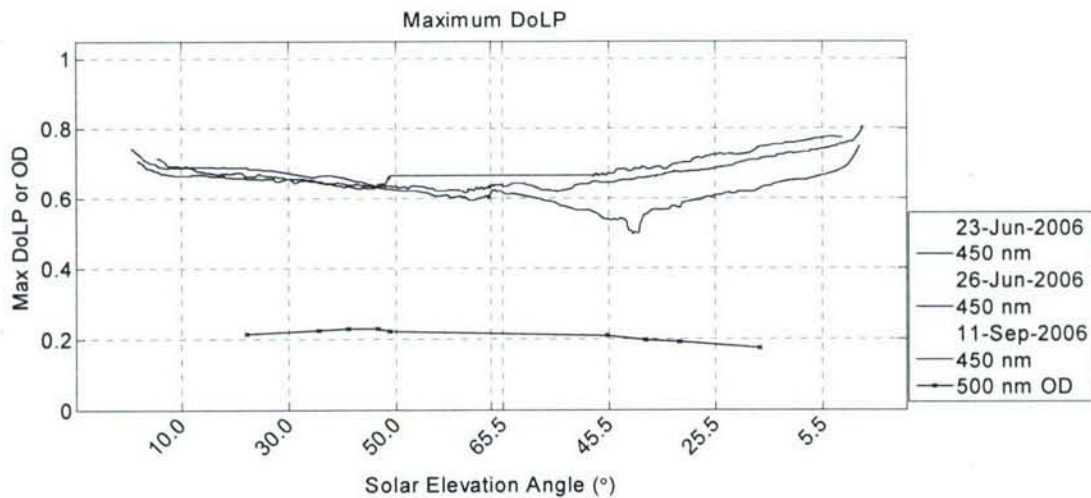
Figure 15. Maximum 450-nm DoLP for June 23, 26 and September 11, 2006. The extra x-axis hash shows the maximum solar elevation for June 23.
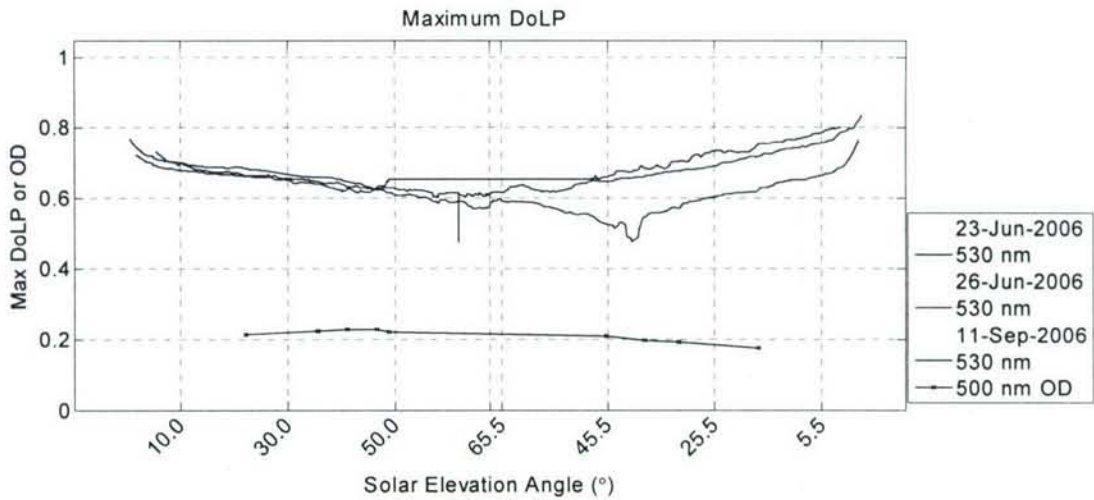
Figure 16. Maximum 530-nm DoLP for June 23, 26 and September 11, 2006 at 530 nm. The flat spot in the September 11 data occurs where the sun never attained that height. The extra x-axis hash shows the maximum solar elevation for June 23.
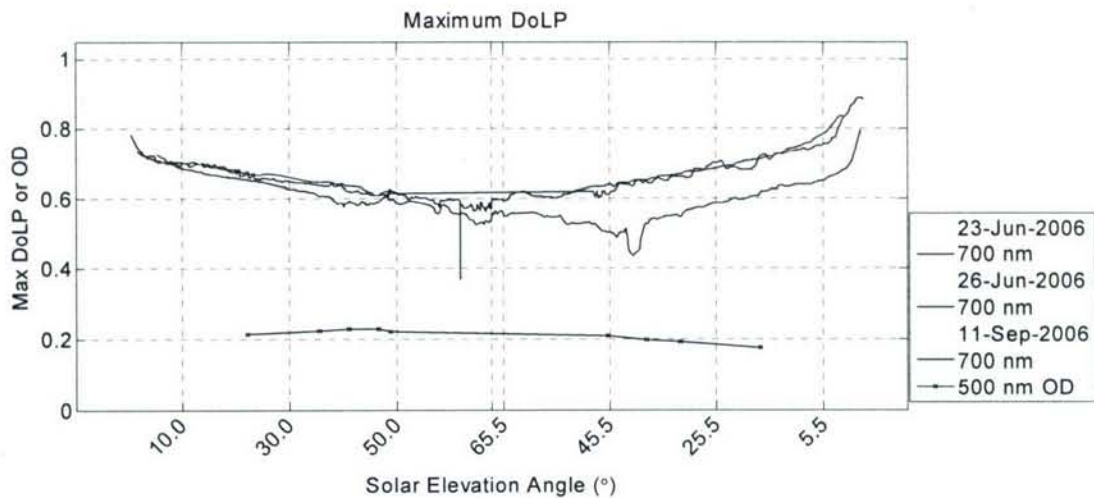
Figure 17. Maximum 700-nm DoLP for June 23, 26 and September 11, 2006. The flat spot in September 11 data occurs when the sun never attained that height. The extra x-axis hash shows the maximum solar elevation for June 23.

We suspect that early stages of cloud formation produce the reduction of polarization observed in clear portions of an otherwise clear sky (in fact, since cloud droplets grow on the aerosols, it begs the question: What is a cloud and what is an aerosol?). This conclusion is supported by the presence of the few small clouds between elevation angles of 31° to 16° (18:00 to 19:27). These clouds are just visible. This conclusion is also supported by the reduction of the maximum degree of polarization

before the clouds are visible in the mid-afternoon. Cloud droplet formation is beginning as the sun moves below 60°, long before the observer perceives clouds.

Therefore, the question must be asked for a partially cloudy sky: Is the sky between the clouds really clear? Although, the sky appears to be clear, this could possibly be a false perception. Thin clouds could be causing the reduction of the DoLP. Therefore, it is uncertain whether the DoLP reduction is caused by either large clouds acting as illumination sources or by thin sub-visual clouds in the apparent clear sky region. Therefore, the optical depth between the clouds needs to be known. For a clear sky, the atmosphere is fairly homogenous. The optical depth measured by a solar radiometer can give an accurate estimate for the whole sky. For obvious reasons, when clouds are present, solar radiometer data cannot predict optical depths across the whole sky. For thin cloud droplet layers seen between the clouds, the same spatial variability problem occurs. To attack this problem, a method of measuring optical depth away from the path to the sun is needed. The best resource for this measurement is a calibrated and steerable LIDAR that can measure extinction. This LIDAR would need the capability to be scanned between clouds. Such instrumentation is presently being developed at Montana State University and is expected to contribute further to this question in future research.

In spite of the difficulties in producing an exact answer to the cause of the DoLP reduction, it is concluded that clouds are highly correlated to a decrease in the degree of polarization between the clouds. One important outcome of this research is the fact that sensors that are used to look down at ground objects through partly cloudy skies will be affected by this reduction of DoLP. The same process that reduces the DoLP between the clouds while looking up will likely reduce the DoLP of a target viewed by a down-looking surveillance instrument. Surveillance aircraft will not be able to look between clouds in a partially cloudy sky without taking into account path scattering between the target and the sensor. Even if other factors are ignored, ground-target signatures will vary considerably between a measurement taken during a clear sky and a measurement taken between clouds in a partially cloudy sky. Furthermore, single-column simulations from P-MODTRAN or any other similar code will be in error unless the actual atmospheric cloudiness, or possibly inter-cloud optical depth, is included in the simulation.

Clouds with non-Zero Polarization

As was seen in the *Partially Cloudy Sky Polarization* section, any measurable DoLP seen when looking at a thick cloud normally arises only from Rayleigh scattering between the cloud and the observer (especially at shorter wavelengths). The Rayleigh scattering into the path overcomes any polarization that a cloud exhibits. Therefore, in these cases the angle of polarization (AoP) seen under the cloud is identical to that of a clear sky, but the bright cloud at the end of the observation path reduces the DoLP. Notice in Figures 18 and 19 that in most areas of the sky, clouds are not even visible in the AoP image. (Areas in black mask areas where the DoLP is under 1%. Since the AoP of unpolarized light is not defined and calibration errors in the fisheye matrix cause errors in the AoP for low DoLP values, these are areas where the AoP data are unreliable.) At longer wavelengths, Rayleigh scattering into the path is minimal. Although the DoLP of the cloud at 700 nm is very low (<5%), the AoP image shows that the polarization angle for some clouds is different than the Rayleigh scattering in the adjacent clear sky (Figure

18). Since a completely unpolarized cloud would reduce the DoLP but not change the AoP, the change in the AoP must come from scattering of the cloud particles themselves. The measurements shown here indicate that clouds themselves can scatter partially polarized light. The typical value of DoLP for this light is less than 5%.

For any single-scattering geometry, the scattering plane is defined by the incident light ray and the scattered light ray. For scattering by particles much smaller than a wavelength, the scattered light will always have a polarization that is perpendicular to the scattering plane. For larger particles, Mie scattering theory predicts that the single-scattered light is polarized in one of two directions: either parallel to the plane of scattering or perpendicular to the plane of scattering. Multiple scattering models have shown little departure from the single-scatter case (Kattawar, 1972). For a line of observation to a cloud, every particle in the line of sight (LOS) will have the same scattering plane, because the plane includes the observer's LOS and the sun. Therefore, all measured polarization angles will either be parallel or perpendicular to this plane. Therefore, the observer sees three primary types of scattering light: (1) Rayleigh scattering in the air between the observer and the cloud, which is always polarized perpendicular to the scattering plane; (2) multiple-scattered light from the cloud droplets, which is primarily unpolarized; and (3) single-scattered light from the cloud droplets which can either be polarized in a perpendicular direction to the scattering plane or in a direction parallel to the scattering plane.

If the single-scattered light from the cloud droplet is perpendicular to the scattering plane, it is oriented in the same direction as the Rayleigh scattered light. For this case, the angle of polarization image will look the same as in the clear sky. When the single-scattered light from the cloud is parallel to the scattering plane and is weaker than the light Rayleigh scattered into the observation path, it will reduce the DoLP as it partially cancels the polarization of the Rayleigh scattering. Still, the AoP will not change. Either of these could describe what is seen in the 450-nm image (Figure 19).

If the scattered light from the cloud droplets is both parallel to the scattering plane and brighter than the Rayleigh-scattered light in the observer's line-of-sight to the cloud, the cloud polarization will overcome the polarization of the light in this path and cause a 90° change in the angle of polarization to occur. This is much more likely to happen at the longer wavelengths since the Rayleigh scattered component is low. Inspection of the AoP image in Figure 21 confirms this explanation, since the clouds are always polarized with an AoP that is oriented approximately 90° from that of the adjacent clear sky. For both images, though, the degree of polarization is very low because the multiple scattering from the cloud is much brighter than both the single-scattered light from the cloud droplets and the Rayleigh scattering between the cloud and the observer.

This concept could be used to check cloud droplet size distributions from other instruments. A Mie scattering code could be used with the predicted droplet size and scattering geometry to predict whether or not the scattered light is polarized at 90° relative to the Rayleigh-scattered light. This prediction could then be compared against

the actual AoP measurement from the polarimeter. Because Mie scattering is strictly valid only for spherical particles, this argument breaks down for ice clouds.

Degree of Linear Polarization   Solar Elev: 35.5
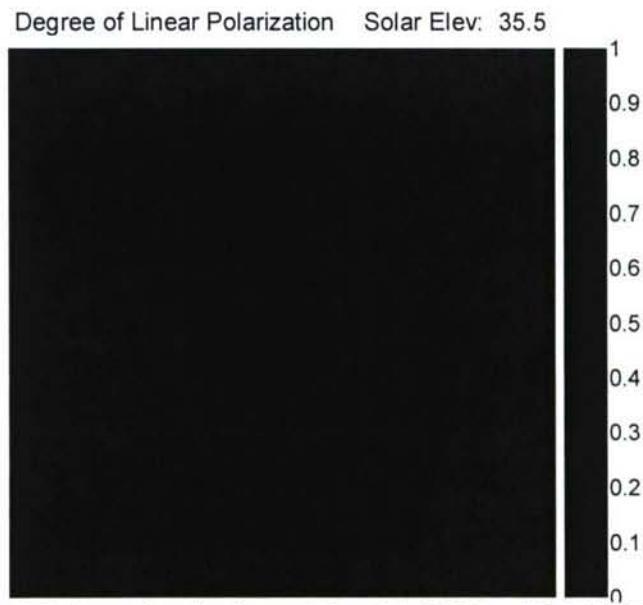
Figure 18. 450-nm DoLP for a cloudy sky on May 24, 2006 at 17:21 MDT.

Angle of Polarization   Solar Elev: 35.5
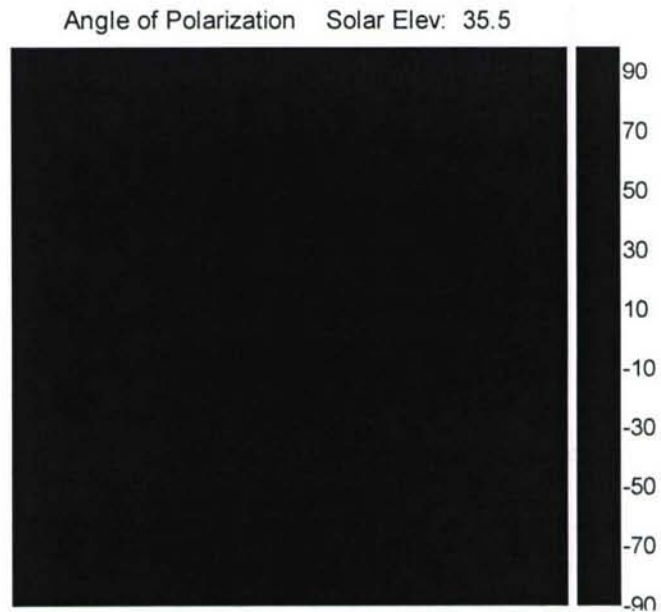
Figure 19. 450-nm AoP for a cloudy sky on May 24, 2006 at 17:21 MDT. Areas in black show areas where the AoP data are unreliable owing to a combination of the AOP being undefined at DoLP = 0 and calibration errors. Areas in black show places where the DoLP is lower than 1%.

Degree of Linear Polarization   Solar Elev: 35.5
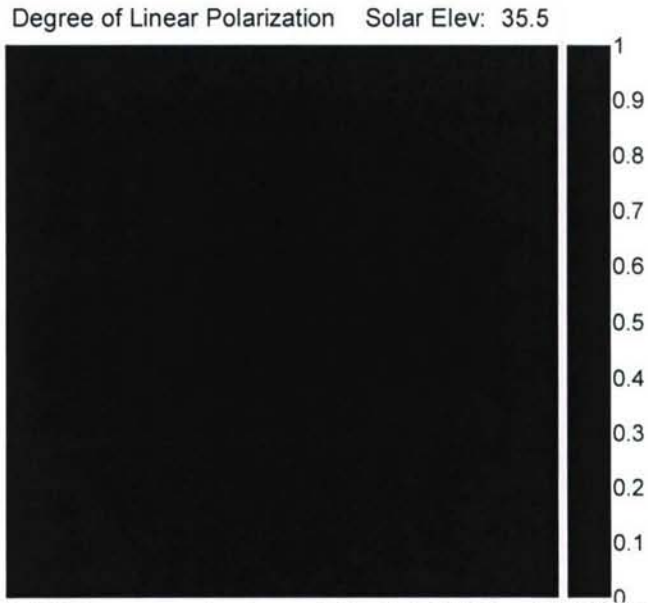
Figure 20. 700-nm DoLP for a cloudy sky on May 24, 2006 at 17:21 MDT.

Angle of Polarization   Solar Elev: 35.5
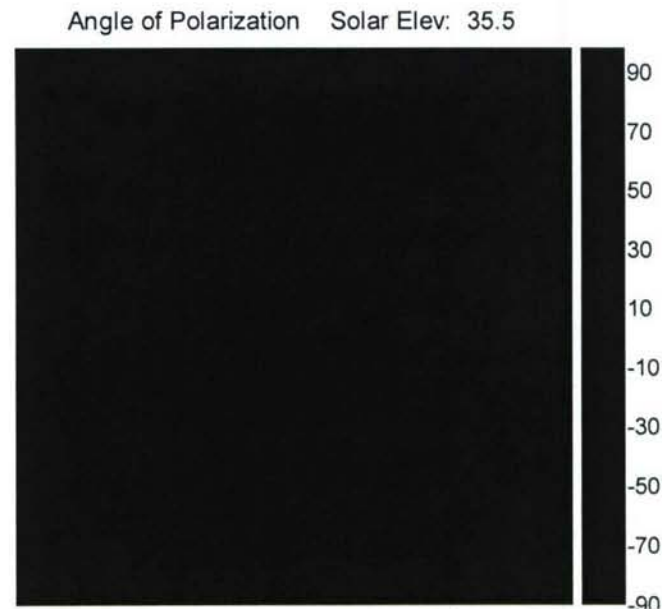
Figure 21. 700-nm AoP for a cloudy sky on May 24, 2006 at 17:21 MDT.

Halo Polarization

On April 12, 2006 between 11:23 and 11:26 MST, a 22° halo was recorded in a full-sky polarization image. The polarimetric images provided a rare opportunity to confirm work done over the last 25 years on the polarization of halos (Können et al., 1983; 1991; 1994; 2003; Lynch, 1979). Although this halo was not complete in any of the three images, almost the entire halo could be assembled from the fusion of the images. The best image taken at 11:24:13 MDT is shown at 450 nm in Figure 22.

One outcome of the previous research on halo polarization has been the assertion that 22° halos will always have a polarization angle that is parallel to the scattering plane—that is the plane that includes the sun, the observer, and the scattering crystal (Können, 1983; 1991). Since the background Rayleigh-scattered skylight will always scatter light polarized perpendicular to the scattering plane, the angle of polarization of the halo will always be oriented 90° from the skylight behind it. Even though noise slightly corrupts the halo AoP image, this characteristic is very clear in the 450-nm AoP image shown as Figure 23.
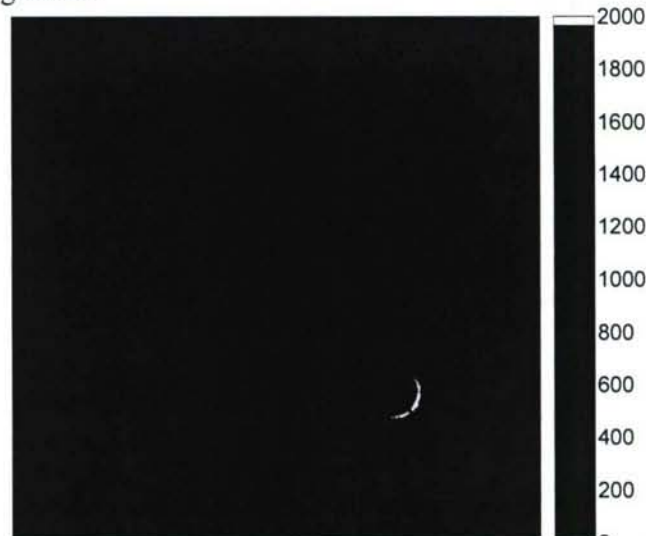
Figure 22. 450-nm Intensity image of a 22° halo at 11:24:13 MDT on April 12, 2006.
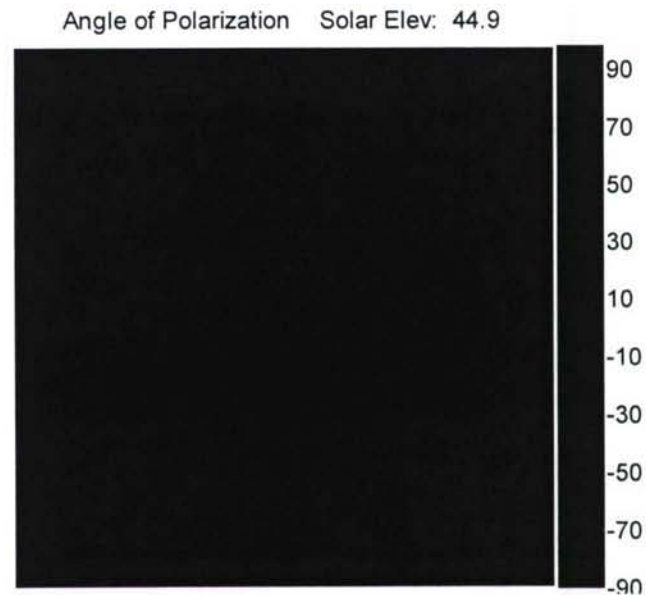
Figure 23. 450-nm Angle of polarization image of a 22° halo at 11:24:13 MDT on April 12, 2006. Areas of low DoLP (<0.8%) are masked in black.

Other wavelengths have similar angle of polarization images. Because of the low exposure needed to suppress bright areas near the sun from overexposure, noise is seen in all DoLP and AoP images. Rescaling of the DoLP images is necessary to see the very low degree of halo polarization. No halo DoLP was above 2%. This was consistent with previous predictions of DoLPs of 4% for 22° halos (Können, 1983) and previous measurements that were below 3% for all wavelengths (Können and Tinbergen, 1991). The lower values in these measurements can be accounted for by the brightness of the background clouds. One difference between the intensity image and the polarization image is the width of the polarized ring. For 450 nm (Figure 24), the ring is much narrower than at 700 nm (Figure 25), which is consistent with previous measurements (Können and Tinbergen, 1991).
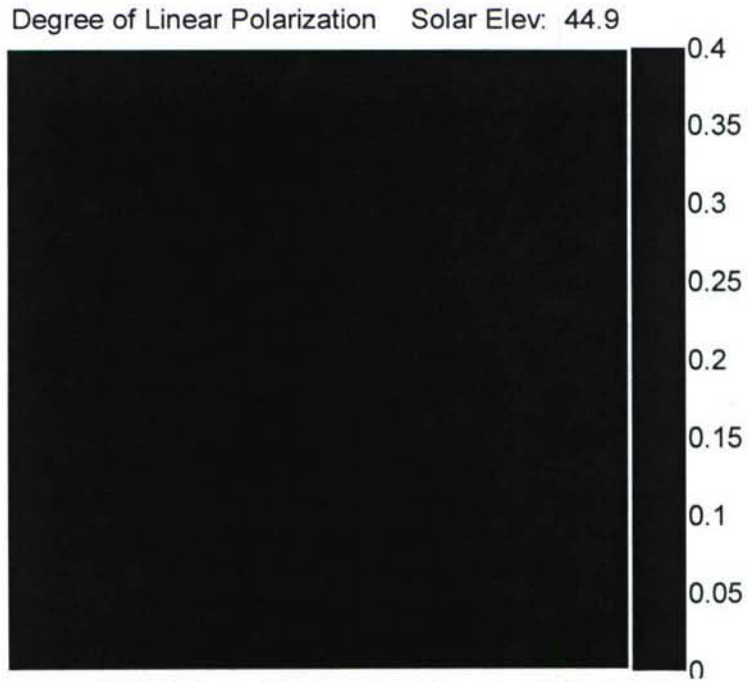
Figure 24. 450-nm DoLP of 22° halo at 11:24:13 MDT on April 12, 2006.

Degree of Linear Polarization   Solar Elev: 44.9
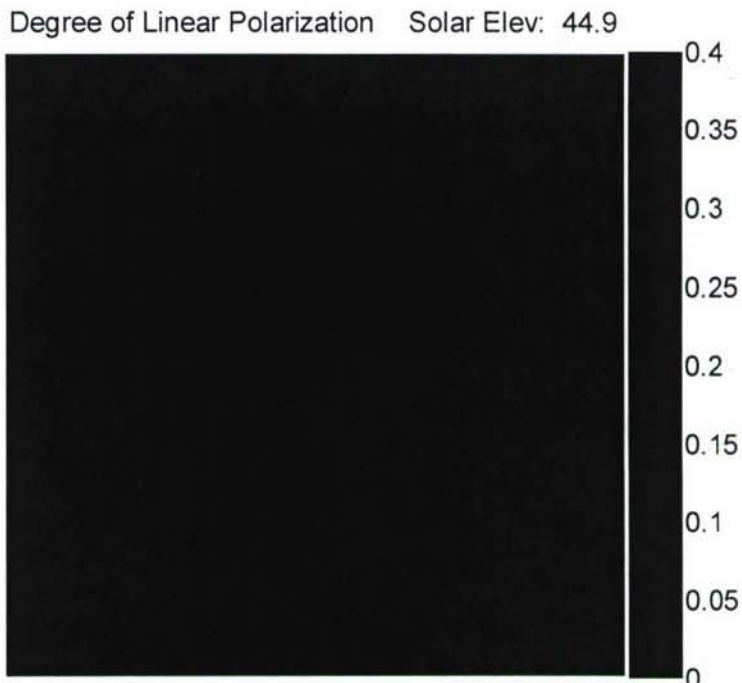
Figure 25. 700-nm DoLP of 22° halo at 11:24:13 MDT on April 12, 2006.

Because of the temporal variability of the halo, there were no data that had the same halo piece in all wavelengths. Therefore, it is difficult to compare the DoLP across wavelengths. Still, the maximum degree of polarization in the ring for each wavelength was found by inspection. The results—although lower than found in previous studies—show a similar trend in DoLP across wavelength. The values for each wavelength are shown in Table 3. These halo polarization images provide valuable confirmation of previous predictions that the halo angle of polarization is parallel to the scattering plane.

Table 3. Maximum Degree of Polarization in the 22° halo.

Wavelength (nm)	Measured DoLP	Konnen 1991 DoLP
450	.010	.026
490	.007	
530	.0091	
630	.0106	
700	.0132	.029

Full-Sky Imaging Polarimetry for Validating P-MODTRAN

One key application of the full-sky imaging polarimeter is to validate the P-MODTRAN code and assess its ability to properly predict the polarization signatures observed in the real atmosphere. Validating the model involves many measured variables.

Each of these variables must be accurate for the validation to be reliable. The validation performed here focuses on the maximum degree of polarization in the clear sky.

Model Input Selection for MODTRAN-P

MODTRAN-P is a versatile tool for modeling atmospheric radiative transfer. It can be used to find atmospheric transmittance spectra, solar irradiance on a surface, effects of surface reflection on satellite measurements, atmospheric thermal emission spectra, etc. Because of its vast applications, the input deck is very complicated with a slew of "cards," optional cards, and optional variables. For this reason, many variables have no bearing on the polarization modeling, but errors in important variables can significantly affect the model. With so many variables, it is easy to lose the important ones among the insignificant ones. Appendix A of Pust (2007) documents the settings that were used in the polarization models given in this study.

Clouds, aerosols, and molecular composition are the three variables that most influence the polarization of scattered light in the atmosphere. Each of these variables must be modeled appropriately to predict the polarization of the sky. MODTRAN uses a maximum of 32 layers in its atmospheric model. The limitation of 32 layers makes modeling fine vertical structures impossible. We launched radiosondes to measure vertical profiles of atmospheric humidity, temperature, and pressure for use in the model. Fortunately, the standard models of molecular composition adequately model the Earth's atmosphere for molecules that do not significantly change in the atmosphere. These standard models include mid-latitude summer, mid-latitude winter, 1976 standard model, etc. Sensitivity of the degree of polarization to changes in the standard model for species other than water vapor was found to be below 0.5%.

Aerosol type and extinction are modeled using four different profiles of separate aerosol classes. These four profiles correspond to the boundary layer aerosol, the tropospheric aerosol, the stratospheric aerosol, and high-stratospheric aerosol. These aerosol classes are each defined with extinction profile, wavelength dependence, and scattering phase function. For each aerosol class, the extinction profile is defined at 550 nm and other wavelengths are determined with a scaling factor from the 550-nm definition. Scattering phase functions for the aerosols can also be defined by the user. In addition, default aerosol profiles for each standard aerosol class are available. These extinction profiles exist for the standard Rural aerosol at 23-km visibility, for the standard Urban aerosol at 5-km visibility, and for the standard Troposphere aerosol at 50-km visibility. Other models are also available. Each standard visibility model contains four typical extinction profiles for each of the four aerosol classes. It is possible to use these standard aerosol models with user-defined extinction profiles for each aerosol class, or even define your own aerosol properties. Also, phase functions can use Mie-generated phase functions, Henyey-Greenstein phase functions, or user-defined phase functions. For this study, aerosol profile extinction information was obtained from solar radiometer and LIDAR data (see the next two sections for details). Dependence of the model on aerosol type was one of the variables tested in the clear-sky models. Without a solar radiometer with more channels or other instrumentation, accurate representations of the aerosol size distribution and phase function could not be derived. Some of these aerosol capabilities

are not available in MODTRAN-P anyway. Therefore, the standard models were used for the aerosol type and the standard Mie-generated database for these models was used for the phase functions, while the extinction profile came from the LIDAR and solar radiometer data. Selecting different standard aerosol models tested the dependence of the model DoLP on the aerosol type.

For clear-sky models, cloud variables were completely turned off in the model. Care was taken to collect data on days that were completely clear of clouds throughout the day for this part of the study—with the exception of September 5, 2006, which had some clouds in the afternoon. For cloudy models, cloud extinction, cloud thickness, and cloud height are necessary inputs to MODTRAN. Cloud extinction is impossible to measure without more sophisticated instrumentation and/or aerial collections. Thickness was modeled according to LIDAR measurements if the cloud was penetrable. Otherwise, the cloud model was not run. Cloud height was obtained from the LIDAR.

The developers of the first release of MODTRAN-P have elected to remove certain capabilities from the original MODTRAN input deck. Since MODTRAN-P is not in full release, these limitations are not consistently documented, yet. The limitations listed below have been found in a few papers and by word of mouth from people close to the project.

Multiple scattering apparently is not properly implemented for polarization. All multiple scattering is modeled as totally unpolarized (Fetrow, 2006). Therefore, inclusion of proper multiple scattering—which is necessary to an accurate model—is impossible. Using multiple scattering in the current code reduces the overall degree of polarization, as it should, but it does so at a rate that is not realistic. The magnitude of this problem is tested in the clear-sky models section.

Only a sub-set of the default aerosol models is available (PPS V4.3 Command Line Usage, 2005). The Navy maritime model, the two fog models, and the desert model are not implemented in the current version. For the simulations here, the Urban, Tropospheric, and Rural models were used for the standard aerosol type.

Finally, this version of the code uses a standard scattering phase function that does not allow the user to achieve realistic modeling for the aerosols present in a particular measurement. Furthermore, it has been shown that improved phase functions will gain nothing for the accuracy of the model until the multiple-scattering algorithms are implemented properly (Conant et al., 2005).

Radiosonde Data – Molecular Extinction Profile

Radiosonde (weather balloon profile information) data were obtained from atmospheric soundings using RS-92 sondes and a Vaisala PP21 Sounding Processor. These soundings provided height, pressure, temperature, and relative humidity profiles. All of these values were directly input into MODTRAN after sampling to the 32 layers used by MODTRAN. These values affect the molecular extinction of the atmospheric profile. Values of molecular components other than water vapor used the defaults of the

Midlatitude Summer model. Layer resampling used an algorithm that sampled for regions of large change in both the relative humidity profile and the aerosol extinction profile extracted from the LIDAR. (Temperature and pressure data did not significantly change compared to the other variables.) Most of the balloons popped at an altitude near 22-27 km. Therefore, the stratosphere was not entirely sampled for relative humidity, pressure, and temperature. Models that ignored the stratosphere consistently under-predicted the degree of polarization in the atmosphere. Because the light scattered from the stratosphere is nearly pure single-scatter Rayleigh, it has a much higher degree of polarization than light scattered in the aerosol-laden troposphere. Since stratospheric Rayleigh scattering proved to be critical to the degree of polarization in the models, a dynamic number of layers (typically around 6 layers dependent upon the altitude that the balloon popped) were reserved for a default stratosphere. The remaining layers were reserved for the radiosonde data.

One surprise found while validating the MODTRAN-P model was that humidity has little effect on the model. When humidity was changed by 10-60%, the degree of linear polarization (DoLP) was affected by less than .01%. Therefore, humidity is not a significant variable--except that it swells the aerosols, but this is accounted for in the optical depth measured by the solar radiometer. It is also possible that changes in the temperature and pressure profile could also be insignificant to the DoLP. Still, using a standard 1976 model as compared to an actual radiosonde profile was shown to cause differences of up to 0.4%. This suggests that using the actual radiosonde data is best, but that standard models may be sufficient in the future. For certainty, the models used here continued to use the real radiosonde data.

Solar Radiometer Data – Total Extinction

Solar radiometry uses measurements proportional to the radiance coming through the atmosphere along with the known detector response for the constant top-of-atmosphere solar radiance to derive the optical depth—or total extinction—of the atmospheric column. A calibrated detector is used to obtain voltages looking directly at the sun. This voltage is then compared to the voltage that the radiometer would see at the top of the atmosphere (determined during calibration) to calculate optical depth. Since the optical depth depends on solar angle, the optical depth calculations are always corrected to an equivalent optical depth for a zenith view (Shaw, 1983).

In addition, the voltage is corrected for the earth-sun distance on the day of the year the measurements were made. All measurements are corrected to an equivalent distance of one astronomical unit (using the square of the Earth-sun distance for r^2 falloff). Adjustments for temperature variation of gain could also be applied, but these sub-percent adjustments were not necessary. Other factors, such as the assumption of atmosphere homogeneity, will contribute more to errors in the models than these small temperature errors.

The solar radiometer, obtained from Dr. Glenn Shaw at the University of Alaska - Fairbanks, measures three different channels—425, 500, and 790 nm. None of the

wavelengths exactly matched the 550 nm extinction profile needed for MODTRAN. However, using the 500- and 790-nm data, the 550-nm optical depth was obtained through linear interpolation. Although the assumption of linear fall off of the aerosols is not valid, aerosol extinctions do change slowly (Schuster, 2006). Also, 550 nm is sufficiently close to 500 nm that the value of the optical depth did not change significantly from the longer wavelength. For most model runs, the correction from optical depth at 500 nm to optical depth at 550 nm was around ~10%. MODTRAN models of transmittance with Rural, Urban, and Troposphere aerosol types showed that the maximum error from linear interpolation would be around 0.3% transmittance. This is a small error compared to other sources of error in the model. The derived 550-nm optical depth was then used to obtain the 550-nm aerosol extinction profile by inverting the LIDAR signal.

LIDAR Inversion – Aerosol Extinction Profile

Although the molecular extinction profile comes from the radiosonde data, aerosol information was also needed to complete the atmospheric profile information. Being one of the key components of depolarization in the atmosphere, aerosol extinction needs to be accurately modeled in MODTRAN-P. The MAML LIDAR system designed and built by Nathan Seldomridge at Montana State University was used to gather back-scatter signal profiles for the aerosols (Seldomridge et al., 2006; Seldomridge, 2006). This LIDAR system uses a laser, a detector, and a sampling analog-to-digital (AD) card to measure the backscatter from the atmosphere. Since the LIDAR sees backscatter from both the molecular components and aerosol components of the atmosphere, an algorithm that both extracts the total extinction of the atmosphere from the signal and separates the aerosol and molecular components of the extinction is necessary. Several methods of LIDAR inversion can be used to extract extinction from a single-color LIDAR signal. Two particular methods of selecting a boundary condition were considered: the far-end solution and the optical-depth solution (Kovalev and Eichinger, 2004).

In the far-end solution, the extinction is assumed to be known for a point in the far end of the LIDAR range. Particularly, it is useful to assume that no aerosols are at a point far above the earth's boundary layer and the LIDAR signal at that range comprise only pure molecular backscatter. In practical inversions, this point is normally taken to be more than 5 km above the earth's surface. Since molecular extinction is easily modeled by a combination of radiosonde data and standard models for the major molecules in the earth's atmosphere, the molecular extinction provides a value for the "boundary"—that is the point of known extinction. The major assumptions associated with this method are: (1) there are really no aerosols at the boundary point far above the earth's boundary layer, (2) the molecular model represents the molecular extinction profile well, (3) the backscatter-to-extinction ratio is known over the profile, and (4) the LIDAR return has a high signal-to-noise ratio (SNR) at the boundary condition point. (If SNR is low at this point, the entire extinction profile can be corrupted by the noise at the range of the boundary condition.) Some of these assumptions may be questionable. For example, without information from other LIDAR wavelengths, the backscatter-to-extinction ratio cannot be known over the profile. For a single-color LIDAR, the backscatter-to-

extinction ratio must take on an assumed value, constant over the LIDAR range. Multi-wavelength lidars can provide additional information (Cattrall et al., 2005) that can be used to improve the estimate of extinction-to-backscatter ratio, but still it nearly always must be assumed to be constant over the entire measurement range unless multiple-angle measurements are made (Spinhirne et al., 1976). Even more, for optically thick aerosols—such as forest-fire smoke—the LIDAR may not penetrate the high aerosol layer. Even if it penetrates the aerosol layer, the SNR can be reduced enough that an accurate boundary condition cannot be formed in the aerosol-free region.

Experimentation with this method showed that using different boundary ranges with a given molecular profile resulted in aerosol profiles that could vary by a factor of 1.5. Noise in the upper ranges caused problems with the boundary condition. For these reasons, this Klett algorithm variant was not used for any of the clear-sky aerosol profile extractions. (A near-end variant of this solution was used for retrieving cirrus extinction. The only difference between these variants is that the boundary value is taken below, not above, the extinction profile of interest in the near-end solution.)

The optical-depth solution uses solar radiometer data to provide the total extinction over the LIDAR range. (Optical depth is the integrated extinction over range.) Since the total LIDAR signal can be integrated and the total extinction is known from the solar radiometer, a relationship is formed between signal and extinction. Using this relationship, the atmospheric extinction profile is determined from the LIDAR signal. If molecular extinction is known, the aerosol extinction profile is then extracted from the atmospheric extinction. Like the far-end solution, the optical-depth solution uses a few assumptions. (1) The optical depth measured by the solar radiometer looking at the sun is the same as the optical depth of the LIDAR looking toward zenith. This assumption equivalently assumes that the atmosphere is homogenous. For models run over the course of a day in areas free of significant aerosol dispersion events, this assumption may lead to a random model error since the aerosols in the direction of the sun will not be systematically higher or lower than the aerosols at zenith. Therefore, it adds to the random noise of the model over the course of the day, but does not induce a systematic error. (2) The optical depth over the LIDAR range is known. This assumption is not trivial since the solar radiometer measures the total extinction to the top of the atmosphere, while the LIDAR only measures up to its maximum reliable operating range (MRR). This range varies and depends upon the amount of path attenuation. For the MAML system, this height could be as low as 2-3 km for extremely optically thick aerosols and upwards of 15 km for clear skies in the daytime. Also, the LIDAR transmit and receive beams are not in full overlap until roughly 70 meters above the surface, so the bottom portion of the profile does not contain accurate signal information. (3) The molecular extinction profile model is accurate. The molecular extinction profile was obtained from the radiosonde data and MODTRAN modeling of the atmosphere without aerosols. (4) Molecular absorption at the LIDAR wavelength is negligible. This assumption is valid at the 530 nm wavelength (Kovalev and Eichinger, 2004). (5) The backscatter-to-extinction ratio is constant over the range and the constant is known. The backscatter-to-extinction ratio for all clear-sky data was set to a constant of 0.016. This value was obtained from Table 7.1 of Elastic LIDAR (Kovalev and Eichinger, 2004, pg.

229). Although the backscatter-to-extinction ratio could vary slightly from this value, the optical depth caused the LIDAR inversion to be bounded. An error in backscatter-to-extinction ratio does not affect the overall extinction of the column, only local variations in the aerosol extinction. (6) There are no thin clouds affecting the solar radiometer measurement. To minimize this affect, clear-sky comparisons were only taken during clear-sky conditions.

Implementation of the optical-depth solution was as follows. A molecular extinction profile was obtained from a MODTRAN model using the radiosonde data. LIDAR data were first processed for offset and range correction. The first dip below zero in the range-corrected signal was used as an indicator of the maximum reliable range (MRR) of the LIDAR. The extinction profile above this range was modeled as a standard Rural 23 km aerosol model. Then, the optical depth above the MRR was integrated from the model results and subtracted from the 550-nm optical depth derived from the solar radiometer data. The resulting optical depth matched the optical depth effectively viewed by the LIDAR.

For the LIDAR inversion, the 550-nm backscatter was assumed to be the same as the 532-nm backscatter. Although this is not exactly true, the more important variable to the MODTRAN model was the total extinction interpolated from the solar radiometer data at 550 nm, not the exact placement of the extinction in the profile. Since the profile is a secondary variable, this is a secondary error and not highly influential on the model. Finally, the ~80 m region below full LIDAR overlap was considered small compared to the ~3 km boundary layer. Therefore, the optical depth measured from the ground level by the radiometer was sufficiently close to the optical depth seen by the LIDAR. In post-processing, the extinction below full overlap was fixed to be the same as the extinction value measured at the first range bin with full overlap (~80 m). LIDAR data inversion followed the forms given in Kovalev and Eichinger, 2004, pg. 175-179. Equations (1) – (2) give the procedure for inverting the signal.

After the aerosol extinction profile was determined, it was resampled to 32 points along with the humidity, temperature, and pressure data using an algorithm that selected ranges with either high humidity or high aerosol extinction changes. An initial MODTRAN model was run and the total optical depth of the molecular and aerosol extinction was calculated from the output. The model optical depth was compared to the 550-nm optical depth derived from the solar radiometer. If the modeled optical depth and the optical depth interpolated from the measured data differed by more than 0.5%, the aerosol extinction profile was rescaled by this factor. Therefore, the optical depth of the MODTRAN model and the solar radiometer always agreed to within 0.5%. This was very important since total extinction (optical depth) seems to be the most important driving variable for polarization. Exact representation of local aerosol extinction in the column is secondary to the inclusion of the true optical depth in the whole model. In fact, other researchers who have done MODTRAN-P validation have completely ignored the column information, using only solar radiometer data to create a homogenous boundary layer model (Conant, 2005). When the LIDAR could not penetrate the boundary layer (~ 3 km above ground), the model was built following a similar approach to these

researchers. For altitudes above the boundary layer, the standard Rural 23 km model was used. The remaining optical depth was spread over a homogenous extinction layer from 3 km down to ground level in the model. The flowchart for the MODTRAN input process is shown in Figure 26. This flowchart only includes the most important steps and ignores minor model variables.
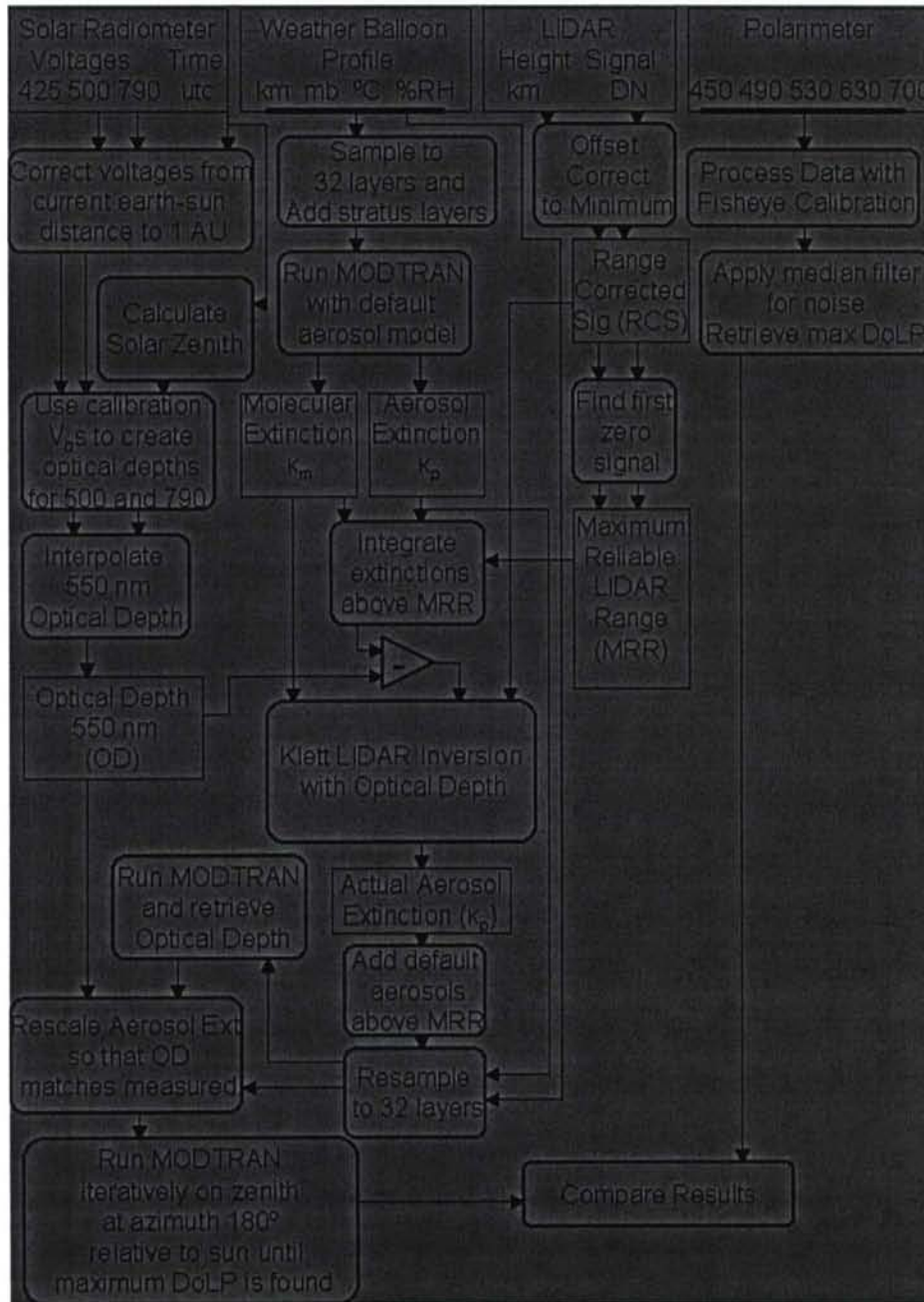

Figure 26. Flowchart of clear-sky MODTRAN-P maximum DoLP comparisons.

Clear Sky Maximum Degree of Polarization Models

While the maximum clear-sky DoLP is not the only parameter than must be validated in the MODTRAN-P simulation, its value is of primary importance to other sky regions. (Clear sky means a sky free of clouds here.) If the maximum DoLP at approximately 90° from the sun is not accurate, the polarization of no other observed zenith and azimuth angles can be expected to be valid. For this reason, the primary focus of this validation work rested upon the maximum DoLP. For both the model and the actual data, the maximum degree of polarization was found. Image processing was used to find the maximum DoLP in the measurements, while an iterative search algorithm found the maximum DoLP for the model. (The maximum model DoLP was always within a few degrees of 90° from the solar zenith angle.)

The model was validated under three different sky conditions: optically thin boundary-layer aerosols, medium-optical-thickness boundary-layer aerosols, and optically thick boundary-layer aerosols. For all sky conditions, the total optical depth (OD) at 500 nm is listed (i.e. the optical depth that includes both aerosol and molecular scattering.) For each sky, MODTRAN-P was run with each of three different standard aerosol types—Rural, Urban, and Tropospheric. The current version of MODTRAN-P only models multiple scattering as completely unpolarized. Therefore, models using multiple scattering were expected to predict a lower degree of polarization than reality. Similarly, single-scatter models were expected to predict a higher DoLP since they do not accurately account for the DoLP reduction by multiple scattering. For each aerosol type, both single-scatter and multiple-scatter models were run to test these hypotheses.

The standard Rural aerosol type represents the closest standard aerosol model to the actual aerosols found in Bozeman during the summer months. These aerosols reflect agricultural processes and a general lack of nearby industrial sources. Still, forest fire smoke in the early part of September lingered during all the days chosen. This smoke, which may contain significant black soot content, may be closer to the standard Urban aerosol than the Rural type. For this reason, these two standard aerosol types—along with the standard Tropospheric aerosol—were chosen for the modeling.

Four questions need to be answered about the MODTRAN-P models. **(1) How accurate are the models? (2) How dependent are the models on aerosol type? (3) Do any of the standard aerosols accurately model all aerosol densities? (4) How accurate are the single-scatter and multiple-scatter versions of the model?**

Note: for all plots in this section, the color of the plotted line closely represents the color corresponding to the wavelength of light for both degree of linear polarization (DoLP) and optical depth (OD)—only total optical depth is reported. Black represents the invisible 700-nm wavelength. All times are Mountain Daylight Time (MDT = UTC-6 hours).

On September 25, 2006, the sky was one of the clearest of the year. By visual inspection of neighboring mountains, only May 31 seemed clearer over the entire summer. Since solar radiometer data were not available for May 31, September 25 was chosen for low-aerosol-content MODTRAN-P validation.

Rural Aerosol Models

Rural aerosol models for the multiple-scatter model are shown in Figure 27. Notice that, when compared to the single-scatter models, the multiple-scatter models are better at preserving the shape of the maximum DoLP curve over the day, especially for the longer wavelengths. Still many problems occur. First, the models for all wavelengths consistently under-predict the maximum degree of polarization in the sky. Secondly, the 700-nm instrument data exhibit the highest DoLP near sunrise and sunset, while in the model the 630-nm data are slightly higher. Finally, during mid-day the model results across the different wavelengths are separated by a larger gap than the measured data, and are ordered differently. Absolute differences between model and instrument results are between 9 and 22% (the instrument calibration uncertainty is approximately ±3%).
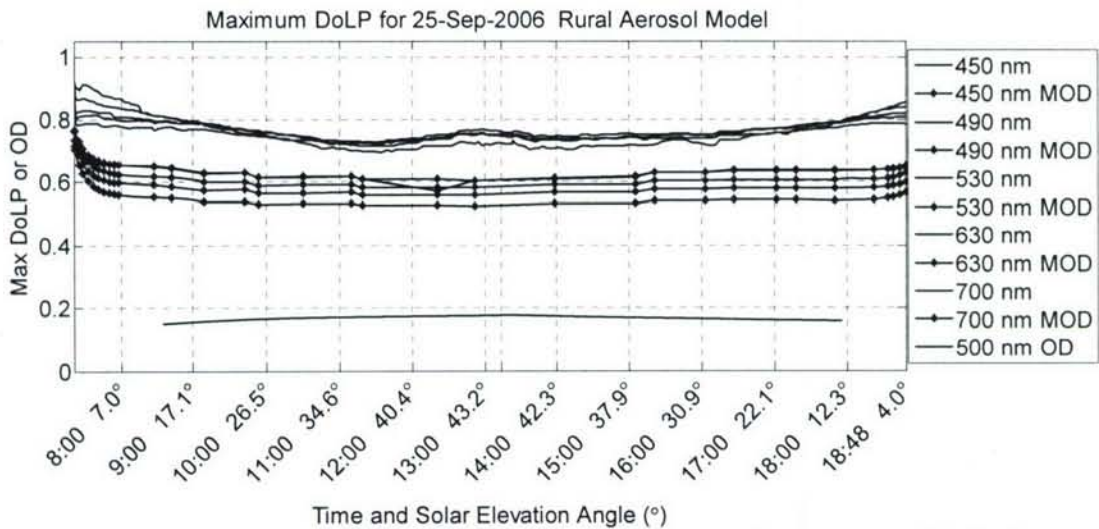
Figure 27. Low-aerosol max DoLP with Rural aerosol multiple-scatter model. Each wavelength is shown using a line color that is similar to the actual color of the light. Dotted lines show the model results (MOD). The 500-nm optical depth measured with the solar radiometer is shown with a green dashed line.
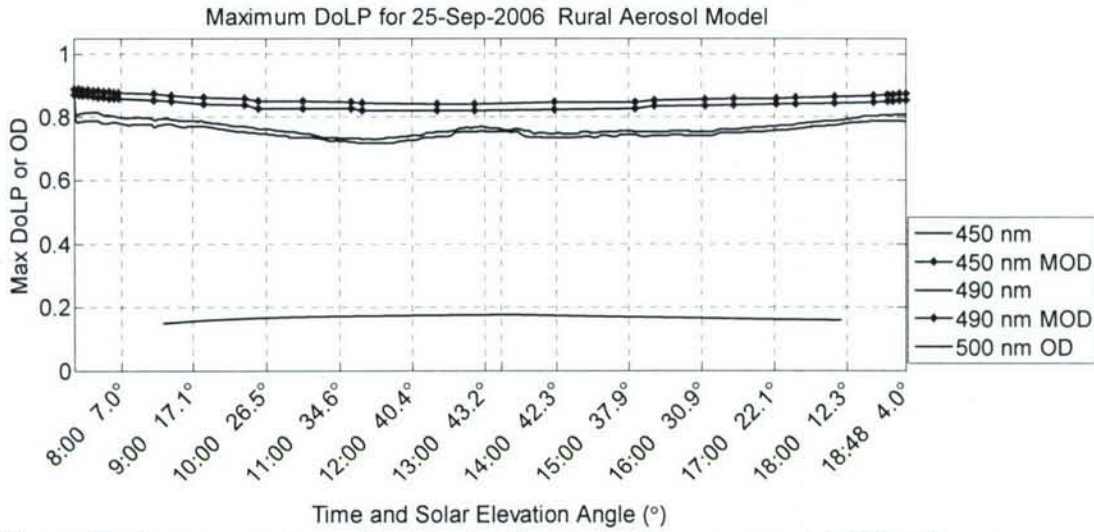
Figure 28. Low-aerosol max DoLP with Rural single-scatter model 450 490 nm.
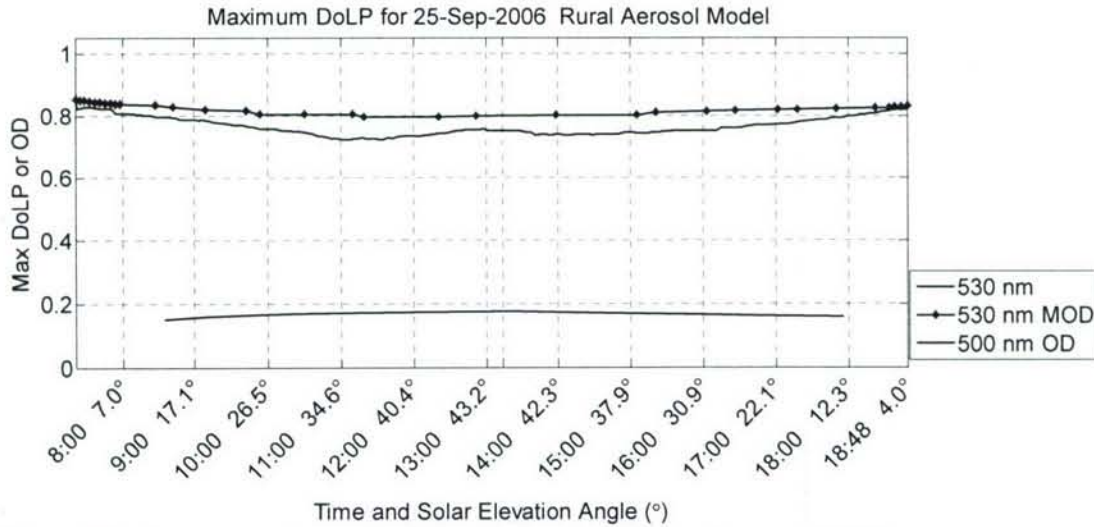
Figure 29. Low-aerosol max DoLP with Rural single-scatter model 530 nm.

For the single-scatter Rural aerosol models, the 450- and 490-nm models are much closer to the measurements, with maximum errors around 13% (Figure 28). The line shape over all solar elevation angles also tracks well. The 530-nm model is even closer with a maximum error of 8% (Figure 29). During mid-day readings, both the 630- and the 700-nm models are within the instrument accuracy (Figure 30 and 31). Still, near sunrise and sunset the model severely under-predicts the values by up to 13%.
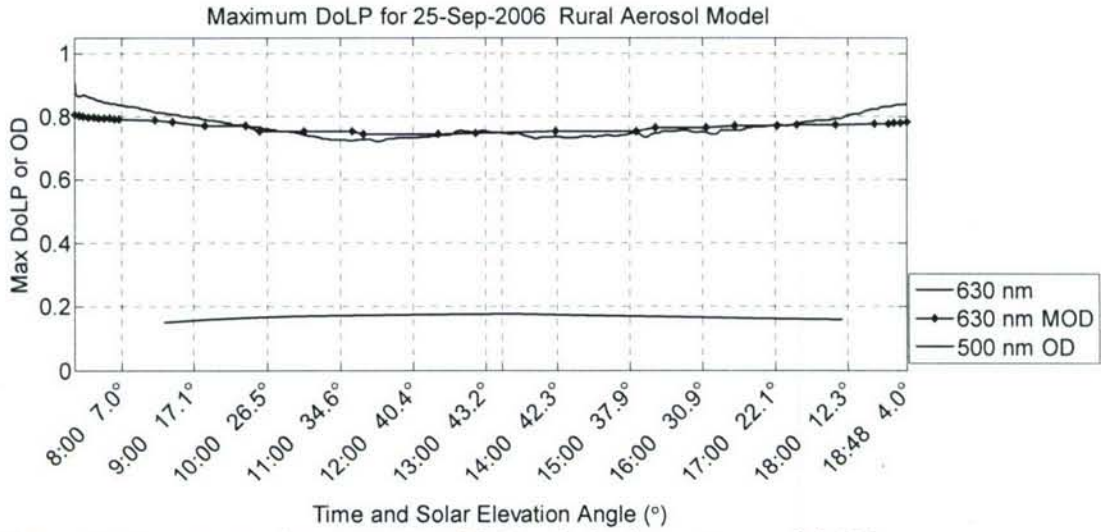
Figure 30. Low-aerosol max DoLP with Rural single-scatter model 630 nm.
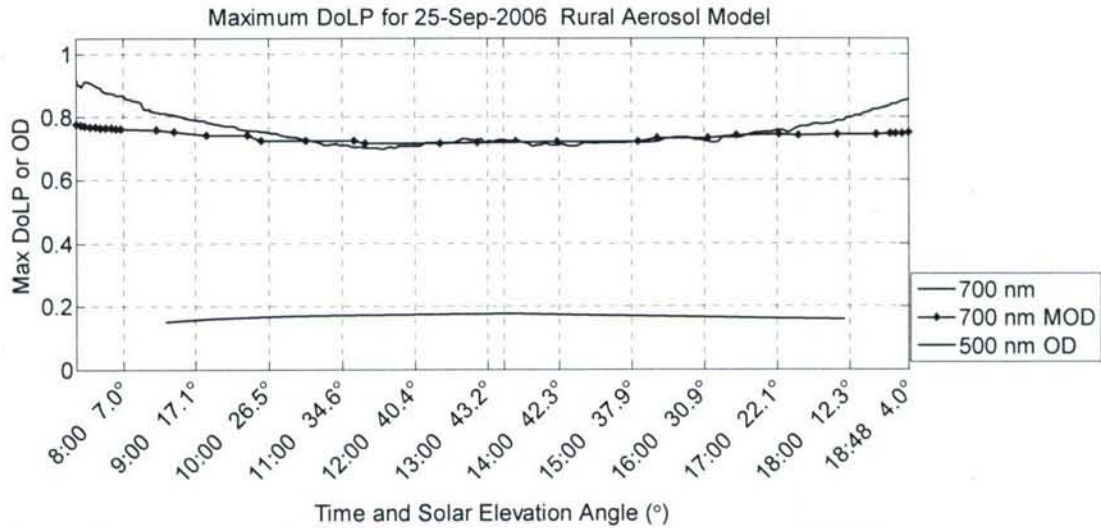
Figure 31. Low-aerosol max DoLP with Rural single-scatter model 700 nm.

Urban Aerosol Models

Urban multiple-scatter models exhibit maximum DoLPs that are nearly identical to the Rural aerosol model, except with a 4% shift toward the instrument data (Figure 32). This may support the assertion that the Urban aerosol model is a better representation of the forest fire smoke seen in the Gallatin valley during September. Similarly, the Urban single-scatter models also increased by about 4% for the long wavelengths and about 2% for the shorter wavelengths. This increase pulls the Urban single-scatter models away from the actual data (Figures 33-36).
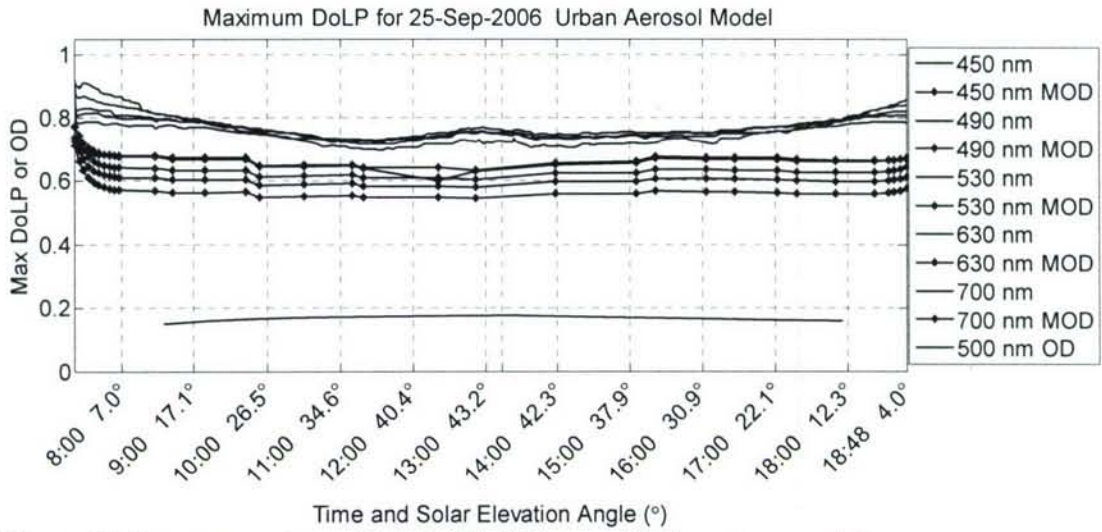
Figure 32. Low-aerosol max DoLP with Urban multiple-scatter model.
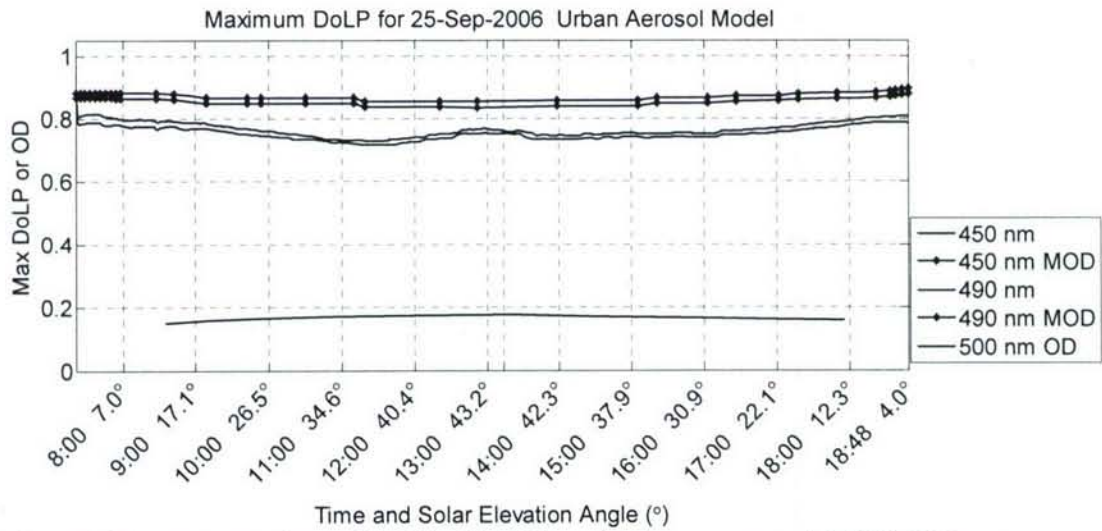
Figure 33. Low-aerosol max DoLP with Urban single-scatter model 450, 490 nm.
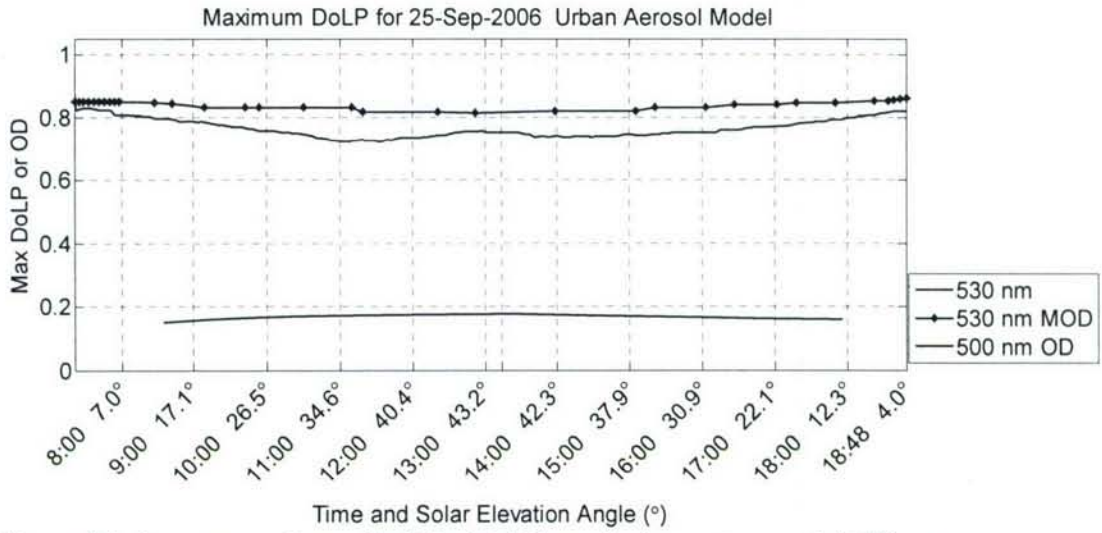
Figure 34. Low-aerosol max DoLP with Urban single-scatter model 530 nm.
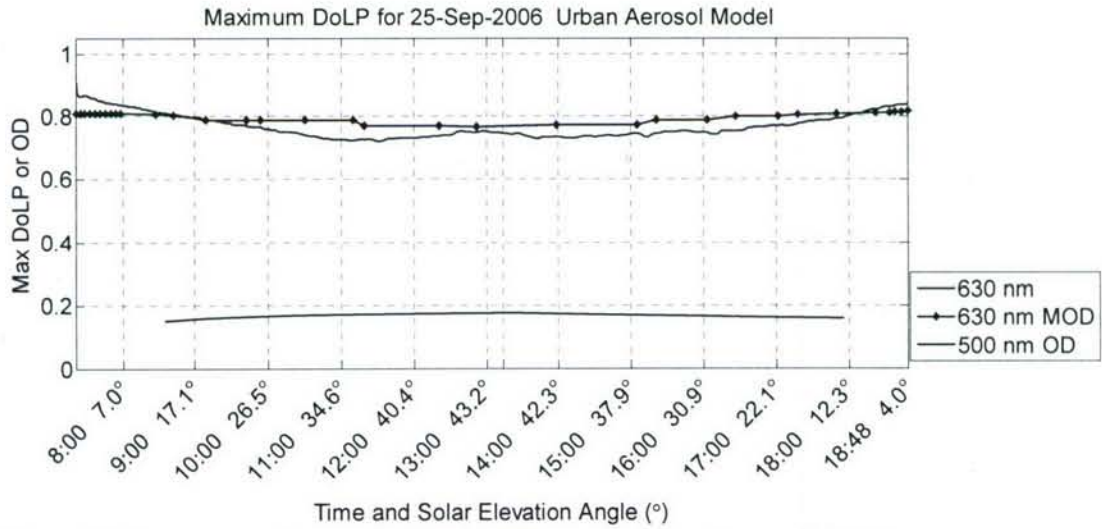
Figure 35. Low-aerosol max DoLP with Urban single-scatter model 630 nm.
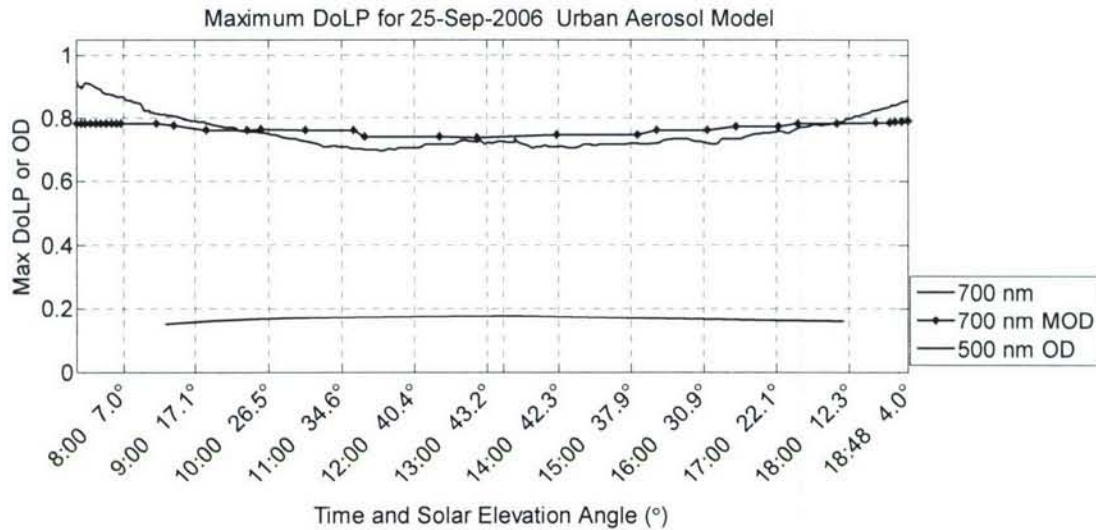
Figure 36. Low-aerosol max DoLP with Urban single-scatter model 700 nm.

Tropospheric Aerosol Models

For most MODTRAN standard models, the boundary layer (< 3km) uses the standard aerosol (Urban, Rural, Maritime, etc.), while the troposphere above the boundary layer uses the standard Tropospheric aerosol. In the standard Tropospheric model, this aerosol type is extended through the boundary layer. Compared with the other two multiple-scatter models, the Tropospheric aerosol type bunches the wavelengths in a more realistic way, but the overall accuracy of the model decreases by ~5% from the Rural model (Figure 37). For the clear sky, this standard aerosol is the worst model for multiple scattering. For the single-scatter models, the shorter wavelengths move the DoLP about 1.5% lower than the Rural model, while the longer wavelengths actually move away from the instrument data. Therefore, the Tropospheric models are worse than both the Urban and the Rural aerosol models for low-aerosol sky conditions.

Maximum DoLP for 25-Sep-2006 Tropospheric Aerosol Model
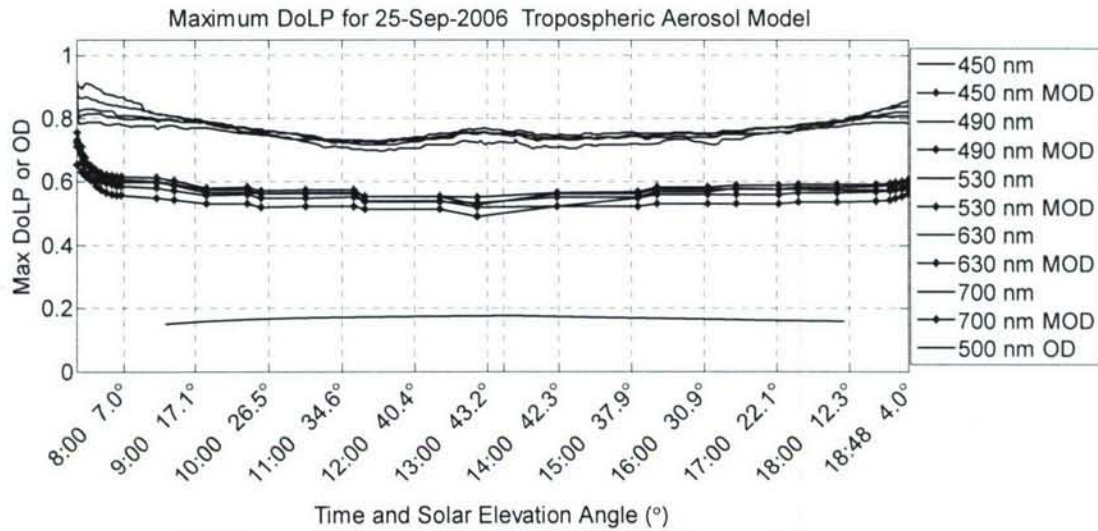
Figure 37. Low-aerosol max DoLP with Tropospheric multiple-scatter model.

The low-aerosol sky models show that the accuracy of the model is greatly dependent upon the type of aerosol used in the model. Although each model has problems with multiple scattering, the single-scatter model is surprisingly accurate when used with the Rural or Urban aerosol type. With the exception of the 450 and 490 nm wavelengths, both of these models predict values during the mid-day that were within the accuracy of the instrument. To better understand the exact accuracy of the model, more instrumentation is needed to measure the aerosol size distribution and MODTRAN-P needs to be upgraded to handle this information. Currently, MODTRAN-P is not capable of handling custom aerosol phase functions (Conant, 2005).

Long-Wavelength Single-scatter Problems

For all standard aerosols, the single-scatter model consistently under-predicts the DoLP near sunset and sunrise. To better understand the problem, the single-scatter model was run without any aerosols. The exclusion of all aerosols and multiple scattering provides an absolute upper limit to the maximum DoLP that can be expected from MODTRAN-P for each wavelength. After the new model was run, the maximum degree of polarization attained from the models was 94%. This was true for all wavelengths, not just the longer wavelengths shown (Figure 38). When multiple scattering and aerosols are removed from the model, only the asymmetries and random distribution of the molecules will reduce the degree of polarization from the 100% value predicted for an ideal spherical Rayleigh scatterer. The value attained by this model is identical to the 94% maximum predicted previously (Bohren, 1996). These data show that the single-scatter model is capable of predicting DoLPs over 90%, so the aerosols in the single-scatter model appear to reduce the DoLP by too much near sunrise and sunset.
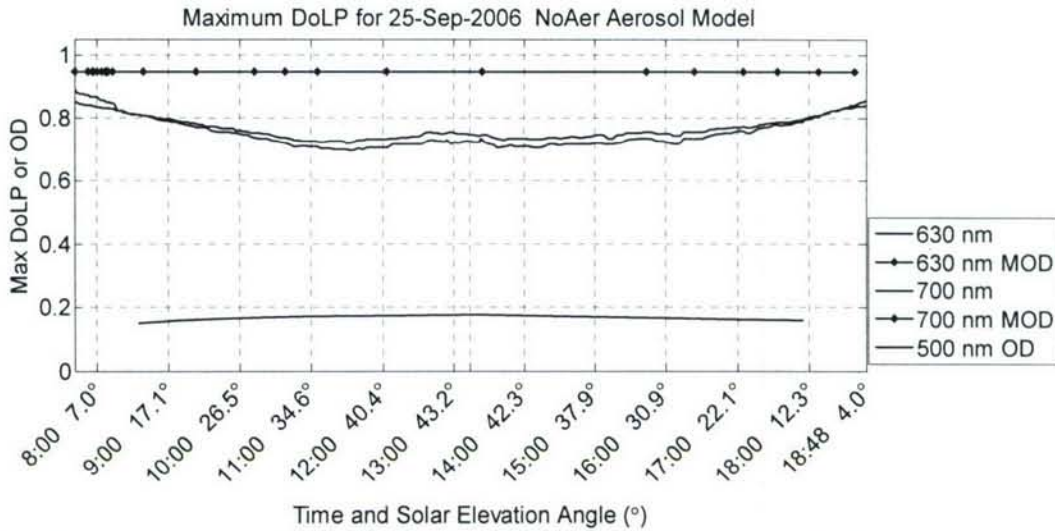
Figure 38. Long-wavelength model without multiple scattering or aerosols

Sky with Moderate Aerosol Content (OD ≈ 0.22)

In late August and early September 2006, forest fires burned in both eastern and western Montana. In particular, fires burned in the Paradise Valley southeast of Bozeman in early September. These fires created some of the worst visibility ever seen in Bozeman on September 5, 2006 (see the next section for data from this day). By September 11, the smoke had cleared considerably and the Tobacco Root Mountains (~70 km away) were barely visible on the horizon. This day provided moderate aerosol data.

Rural Aerosol Models

Figure 39 shows the results of the aerosol models with multiple scattering. For this day, the aerosols dropped significantly over the course of the afternoon and the model tracks appropriately. Still, the multiple-scatter model consistently under-predicts the DoLP. Also, notice that the order of the different wavelength plots is still inverted—with the 700-nm wavelength staying the highest during mid-day.
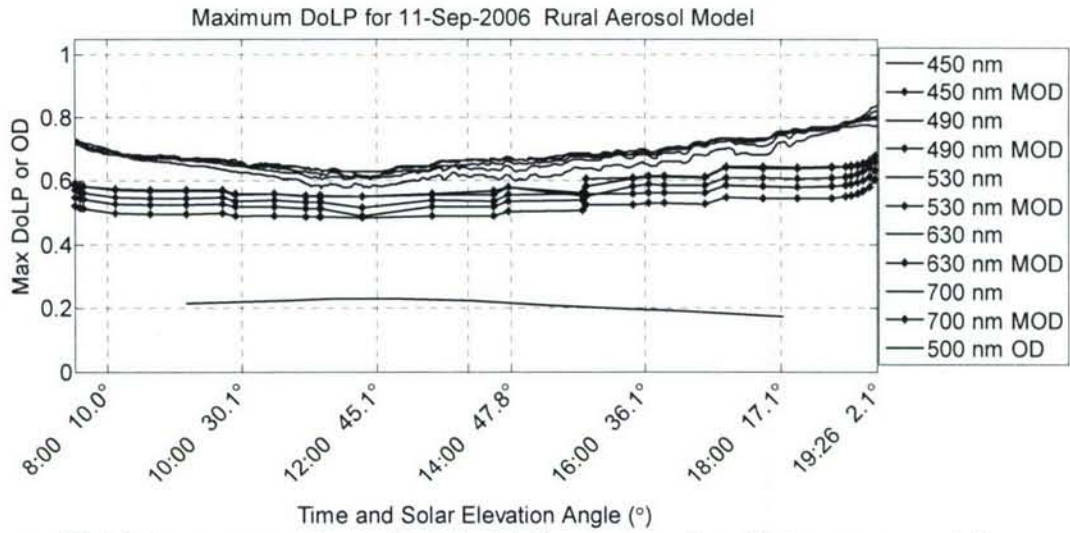
Figure 39. Moderate-aerosol max DoLP with Rural aerosol multiple-scatter model.

With moderate aerosols, single-scatter models over-predict the DoLP for all wavelengths (Figures 40-41). This is a departure from the low-aerosol Rural models, which predict the longer wavelengths well.
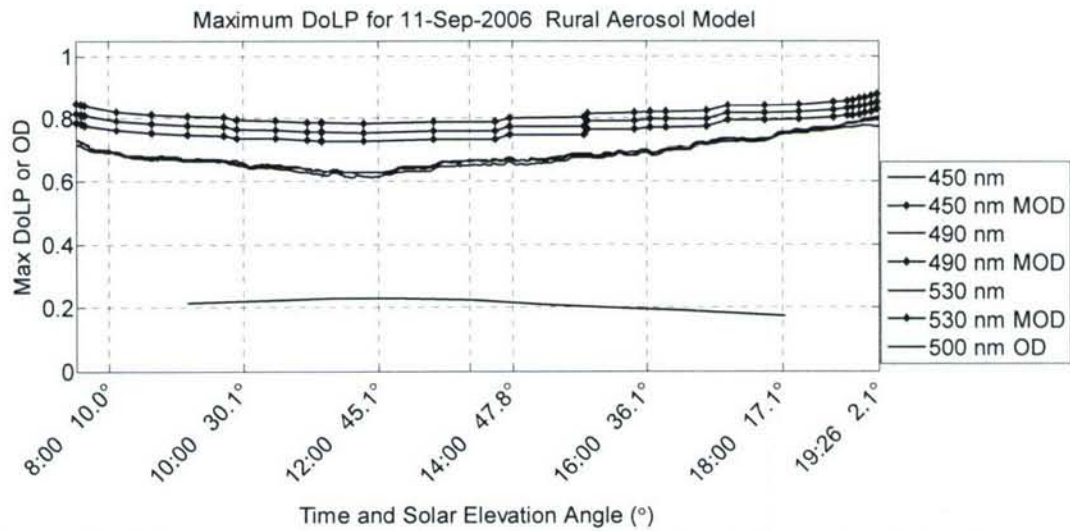

Figure 40. Moderate-aerosol max DoLP with Rural single-scatter model 450-530 nm.
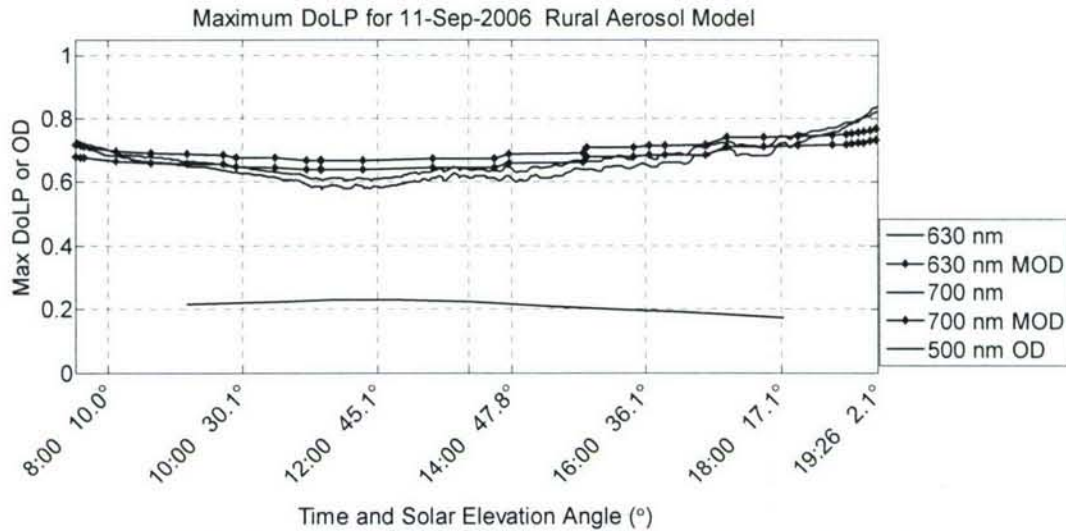
Figure 41. Moderate-aerosol max DoLP with Rural single-scatter model 630, 700 nm.

For the mid-day clear sky, a single-scatter model seems to be adequate for the longer wavelengths, but as aerosols increase, the scattering in the boundary layer causes the model to separate from the actual data. Notice that as the optical depth at 500 nm begins to drop below 0.20, the single-scatter 630-nm and 700-nm models become accurate to within the instrument accuracy, but above this point they diverge from the instrument. The errors for 630 and 700 nm have now become as much as 7% during the mid-day, while the shorter wavelengths are worse than the low-aerosol models.

Urban Aerosol Models

Urban models are shown in Figures 42-44. For the multiple-scatter model, the results are almost identical to the Rural model. The Urban model runs about 1% lower than the Rural model for most wavelengths. The single-scatter Urban models are similar to their Rural counterparts, but in all cases, they over-predict the measured DoLP to a larger extent than the Rural models.
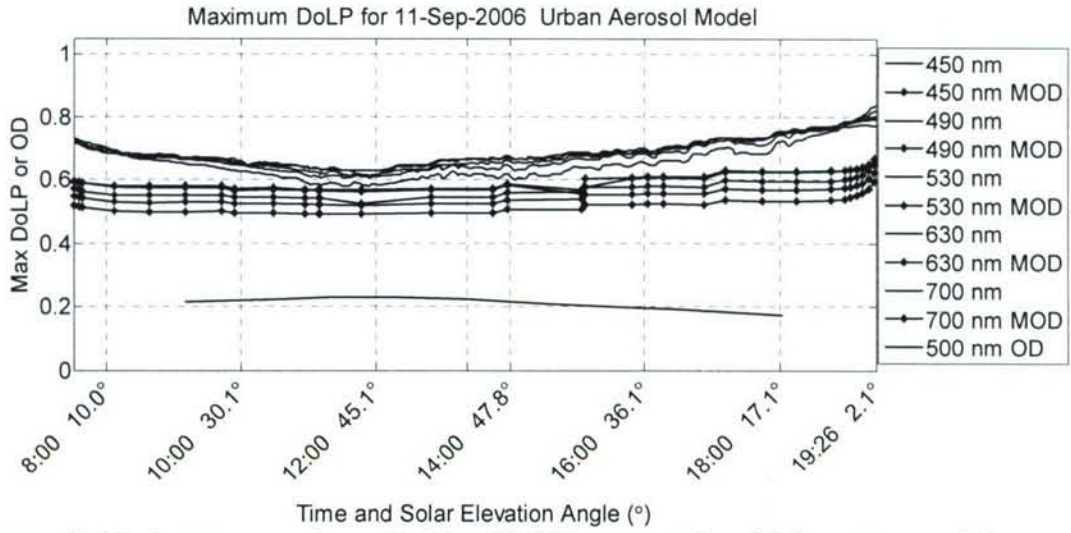
Figure 42. Moderate-aerosol max DoLP with Urban aerosol multiple-scatter model.
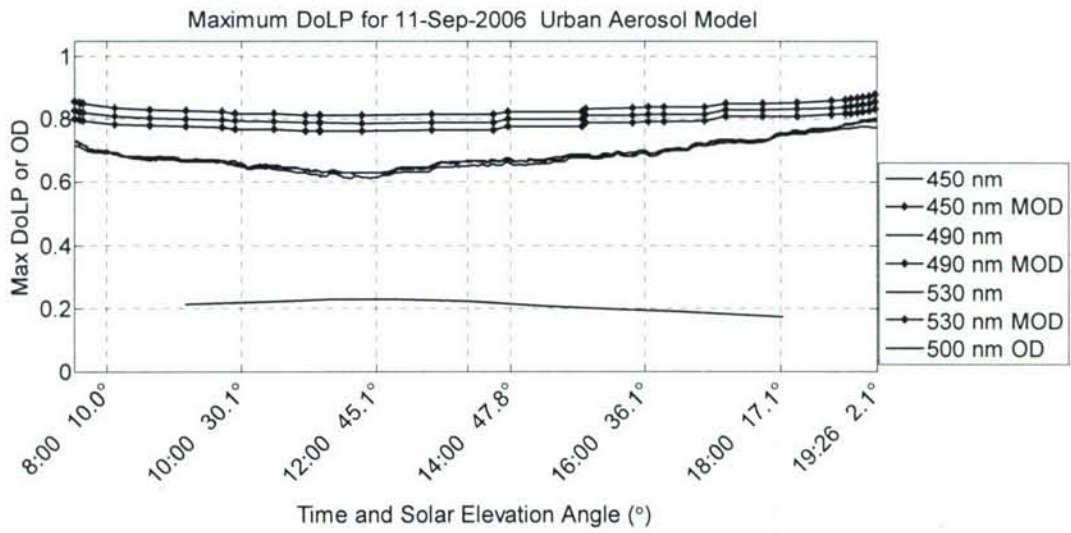
Figure 43. Moderate-aerosol max DoLP with Urban single-scatter model 450-530 nm.

Maximum DoLP for 11-Sep-2006 Urban Aerosol Model
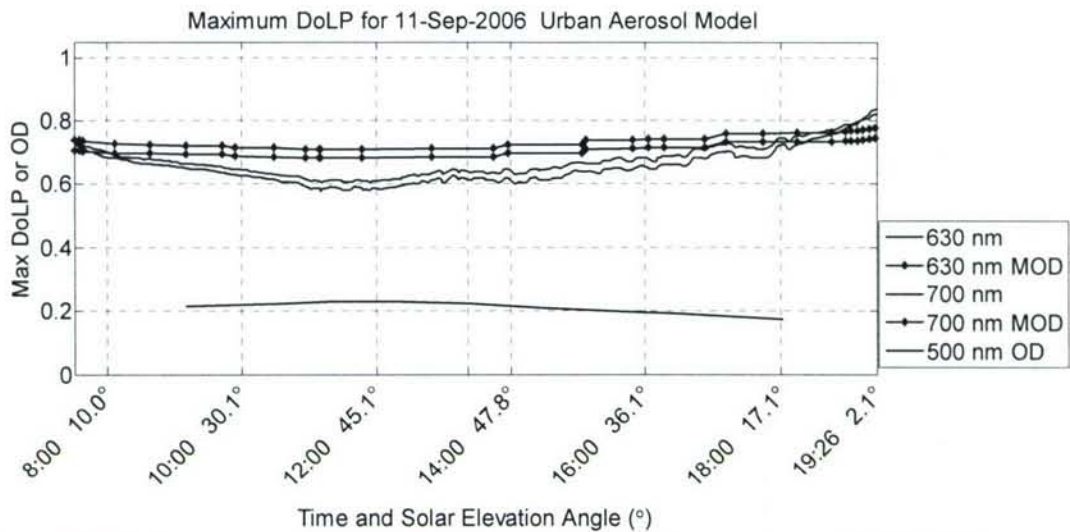
Figure 44. Moderate-aerosol max DoLP with Urban single-scatter model 630, 700 nm.

Tropospheric Aerosol Models

Finally, the Tropospheric models are shown in Figures 45-47. Similar to the low-aerosol sky case, the Tropospheric aerosol type produces much lower model maximum DoLP than the Urban and Rural types for the multiple scatter models. For the single-scatter models, the Tropospheric aerosols ran closer than the other aerosol types. The better accuracy of the single-scatter Tropospheric aerosol type is probably coincidence, not a reflection of the overall accuracy of the model. The higher reduction of the DoLP by the Tropospheric aerosol model is compensating for the over-prediction of the single-scatter model.

Maximum DoLP for 11-Sep-2006 Tropospheric Aerosol Model
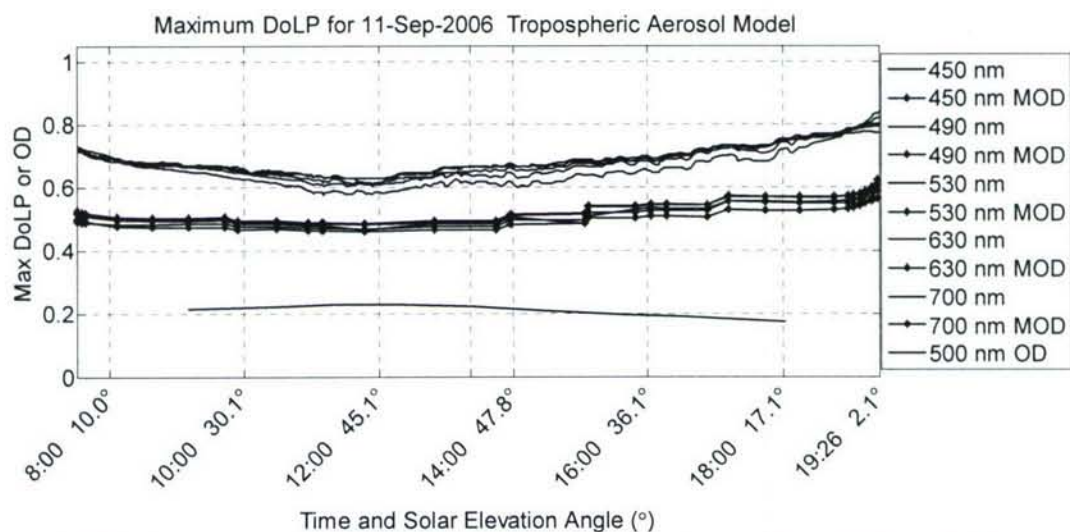
Figure 45. Moderate-aerosol max DoLP with Tropospheric multiple-scatter model.
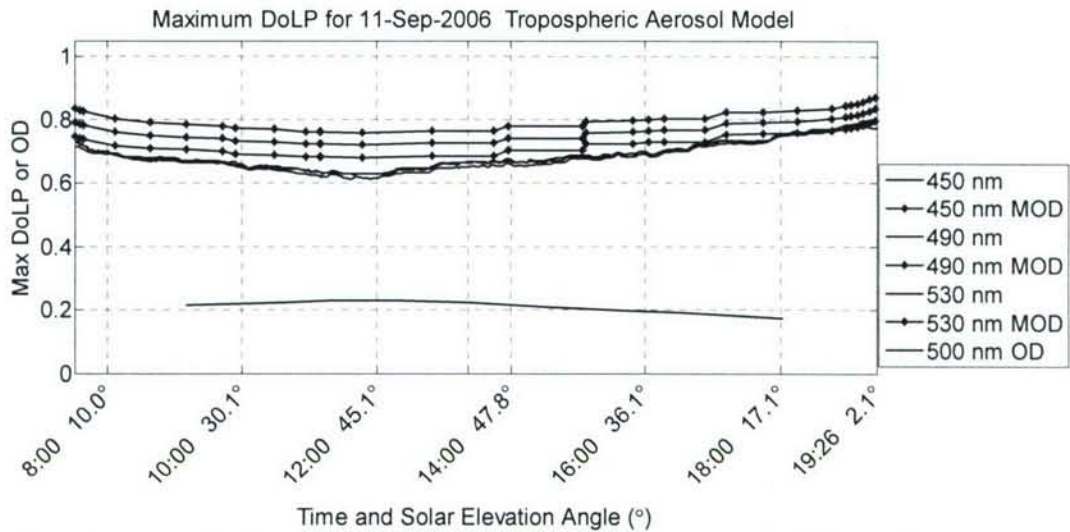
Figure 46. Moderate-aerosol max DoLP with Tropospheric single-scatter model 450-530 nm.
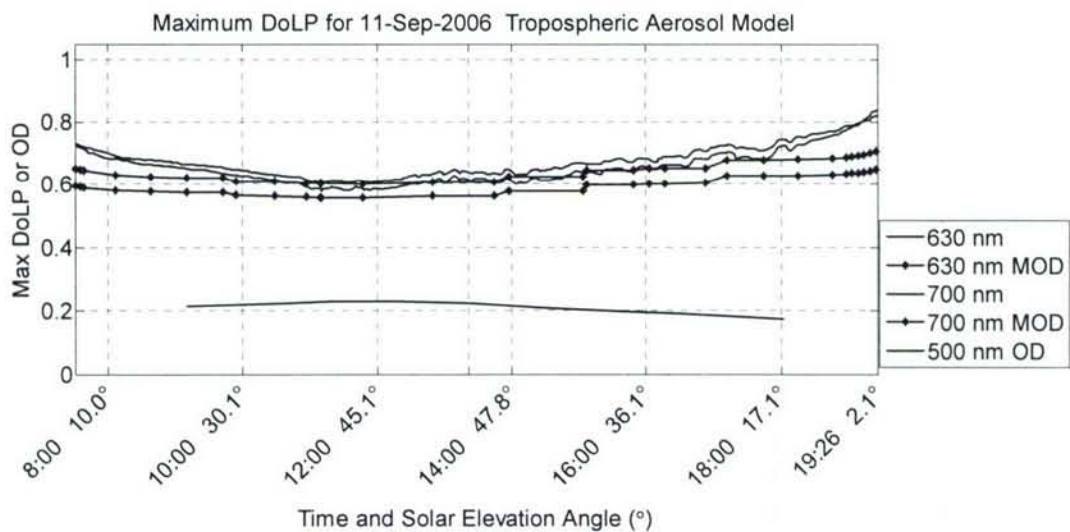
Figure 47. Moderate-aerosol max DoLP with Tropospheric aerosol single-scatter model 630-700 nm.

High-Aerosol-Content Atmospheric Conditions (OD ≈ 1.2)

September 5, 2006 provided a very dense aerosol layer—one of the worst Bozeman has ever seen. At some points in the afternoon, visibility on the ground was below 1.5 km. Only afternoon data were taken on this day. The bump in the data around 14:30 is from clouds that formed in the early afternoon. These clouds are seen in the data taken around this time. It is assumed that even the thinnest clouds went away later in the afternoon, but visibility was bad enough that it is unknown how many thin clouds were really above the aerosols. The optical depth is not shown in the figures since it is off

scale. It slowly moved from 1.34 at 12:50 to 1.00 at 16:39. Later in the day it slowly increased to 1.25 at 18:10.

Rural Aerosol Models

Figures 48 and 49 show the multiple-scatter models for the high-aerosol day. For clarity, the shorter wavelengths have been separated from the longer wavelengths. The multiple-scattering model consistently under-predicts the DoLP. During the mid-day, the long-wavelength errors are as much as 20%, while the shorter wavelengths are inaccurate by 10%.
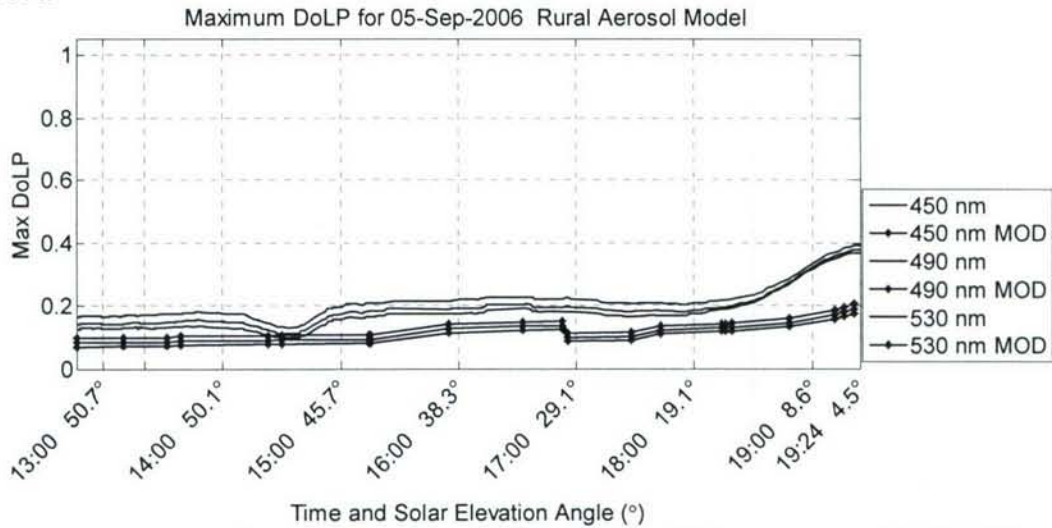

Figure 48. High-aerosol max DoLP with Rural aerosol multiple-scatter model 450-530 nm.
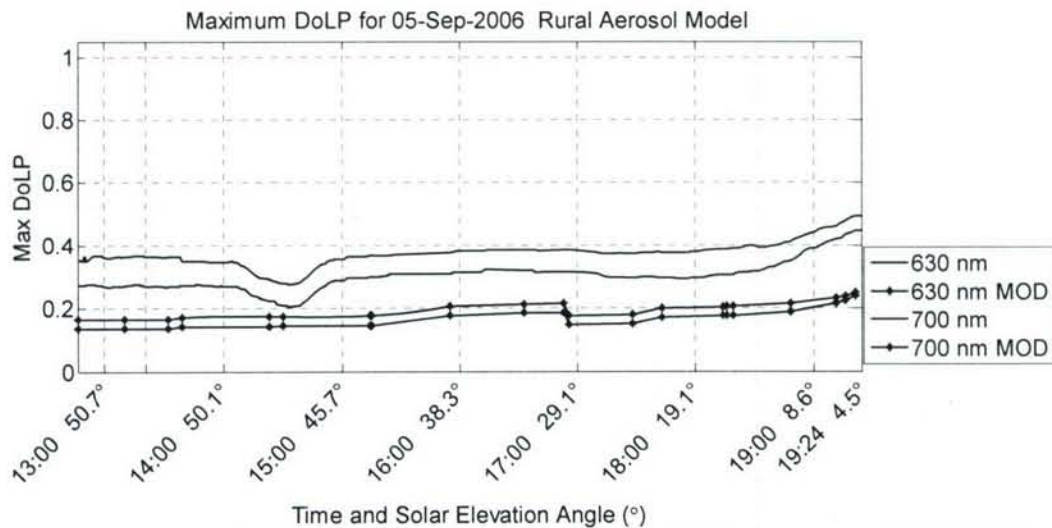
Figure 49. High-aerosol max DoLP with Rural aerosol multiple-scatter model 630, 700 nm.

Single-scatter models exhibit characteristics similar to the other models. Short wavelengths are not even close (Figure 50). Surprisingly, the largest error in the 700-nm wavelength model is only 6% (Figure 51).
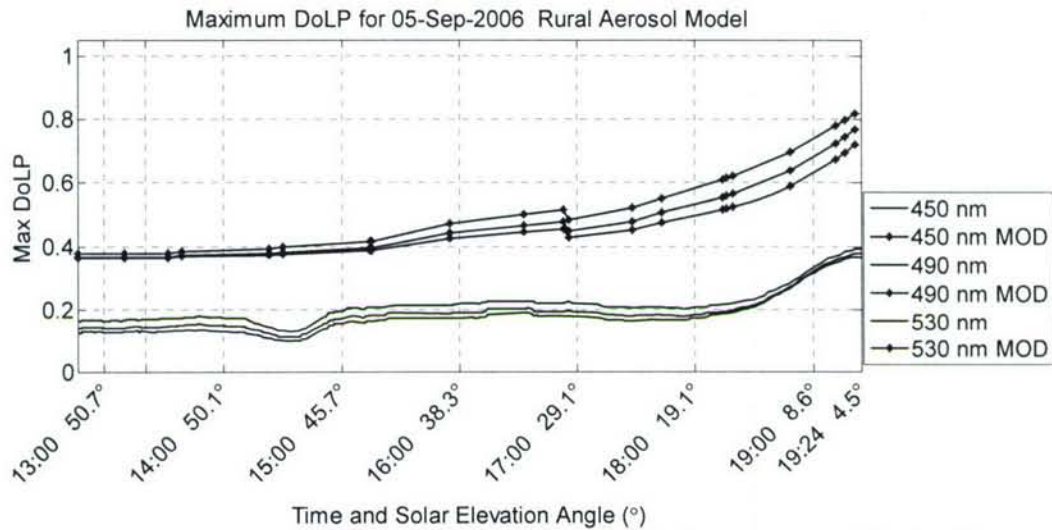

Figure 50. High-aerosol max DoLP with Rural aerosol single-scatter model 450-530 nm.
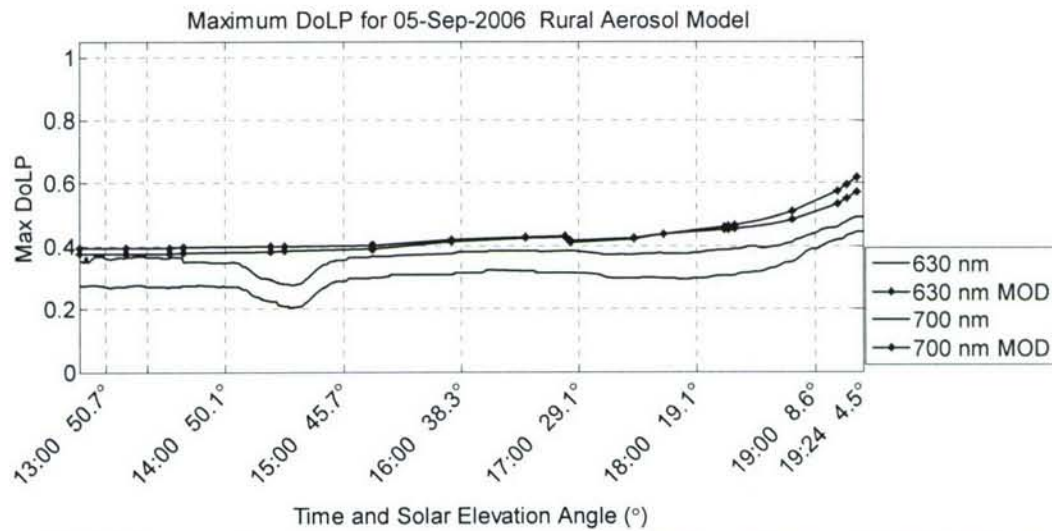
Figure 51. High-aerosol max DoLP with Rural aerosol single-scatter model 630, 700 nm.

Urban Aerosol Models

For all Urban multiple-scatter models, data were within 6%, except near sunset (Figure 52-53). These short-wavelength Urban cases are the only ones across all the models for which the multiple-scatter model is above the measured DoLP. Since the multiple scattering is modeled as unpolarized, all models should be below the actual data. This suggests that either the Urban aerosol is a bad representation of the September 5

forest fire aerosols, or another problem with the MODTRAN-P code exists. As with the Rural models, the single-scatter Urban models are always very bad (Figures 54-55).
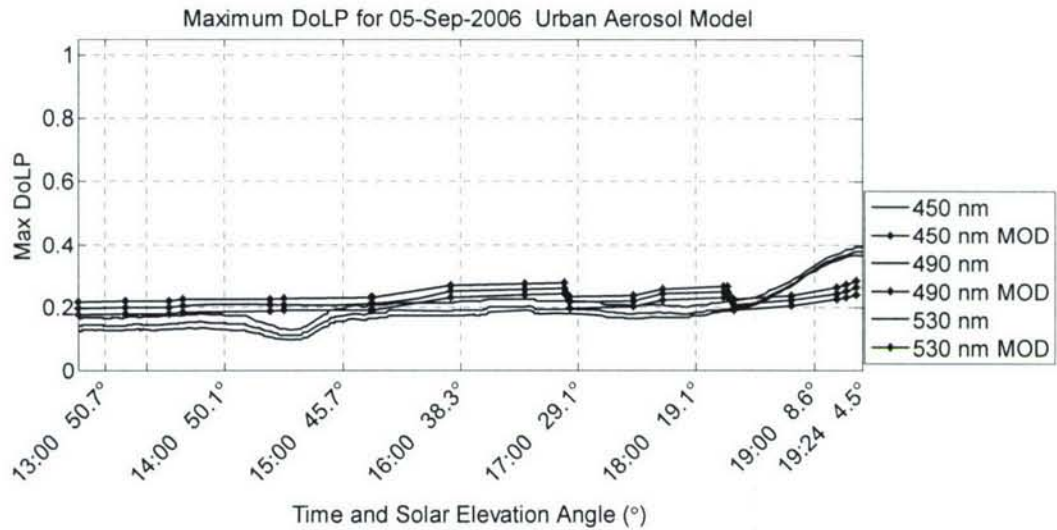

Figure 52. High-aerosol max DoLP with Urban aerosol multiple-scatter model 450-530 nm.
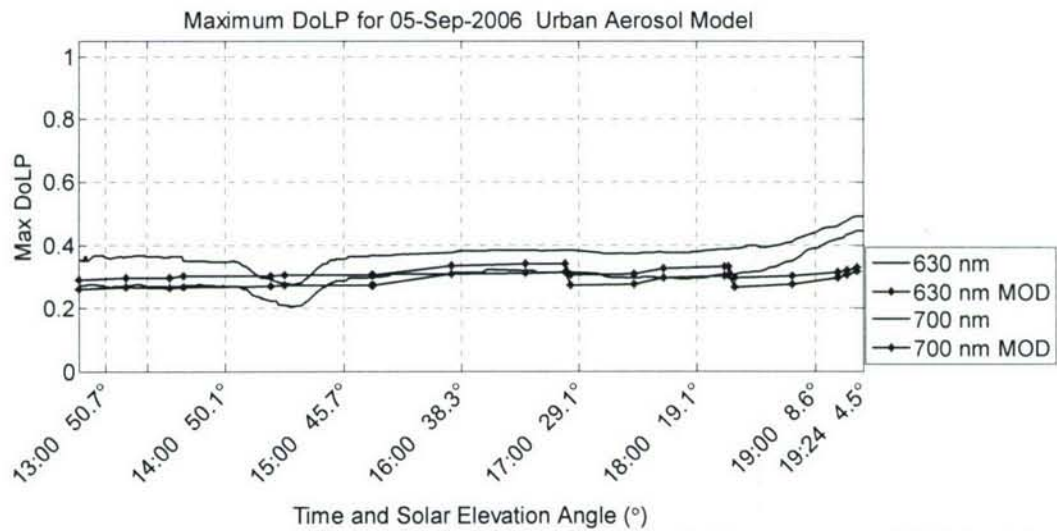

Figure 53. High-aerosol max DoLP with Urban aerosol multiple-scatter model 630, 700 nm.
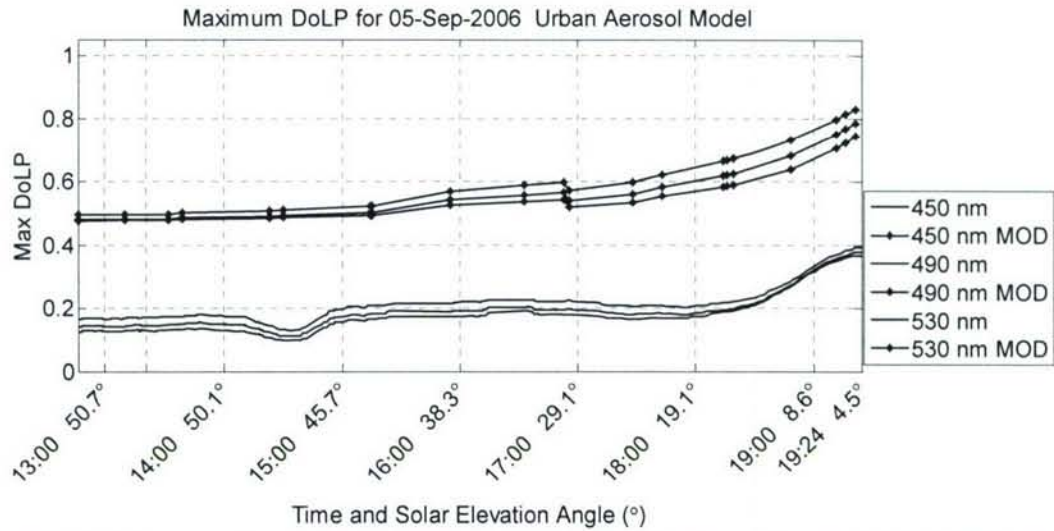
Figure 54. High-aerosol max DoLP with Urban aerosol single-scatter model 450-530 nm.
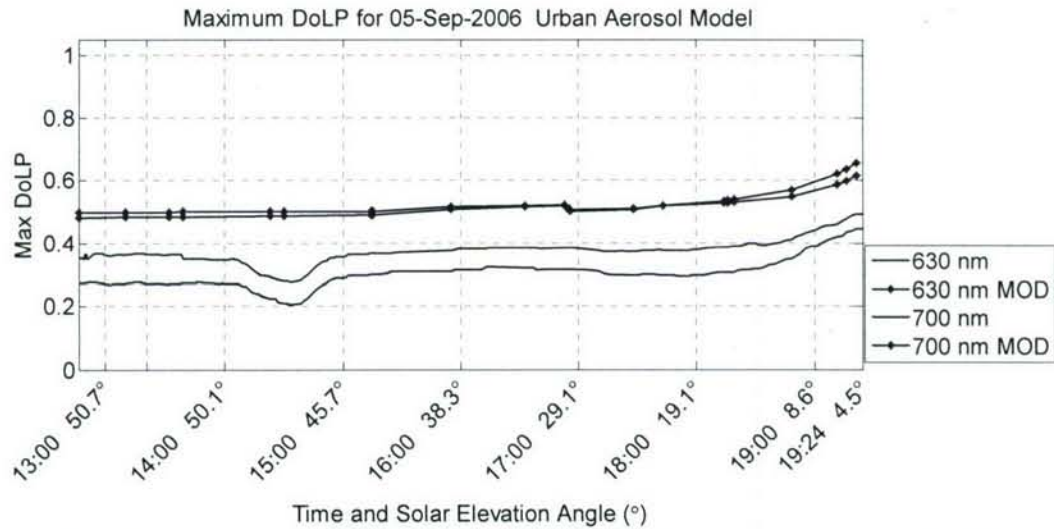

Figure 55. High-aerosol max DoLP with Urban aerosol single-scatter model 630, 700 nm.

Tropospheric Aerosol Models

Tropospheric aerosols did not perform any differently than the previous Tropospheric models (Figures 56-59). Multiple-scatter predictions were too low. Single-scatter short wavelength predictions were very bad, but the longer wavelengths were within 5%. Again, this is probably a result of the competing processes—the high polarization prediction of the single-scatter model against the too-severe DoLP reduction by the Tropospheric aerosol.
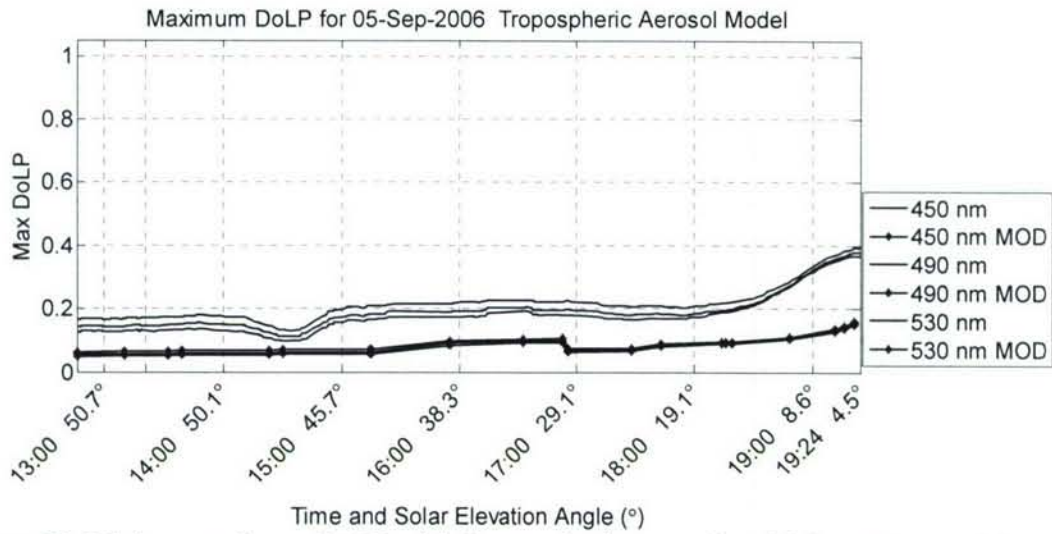
Figure 56. High-aerosol max DoLP with Tropospheric aerosol multiple-scatter model 450-530 nm.
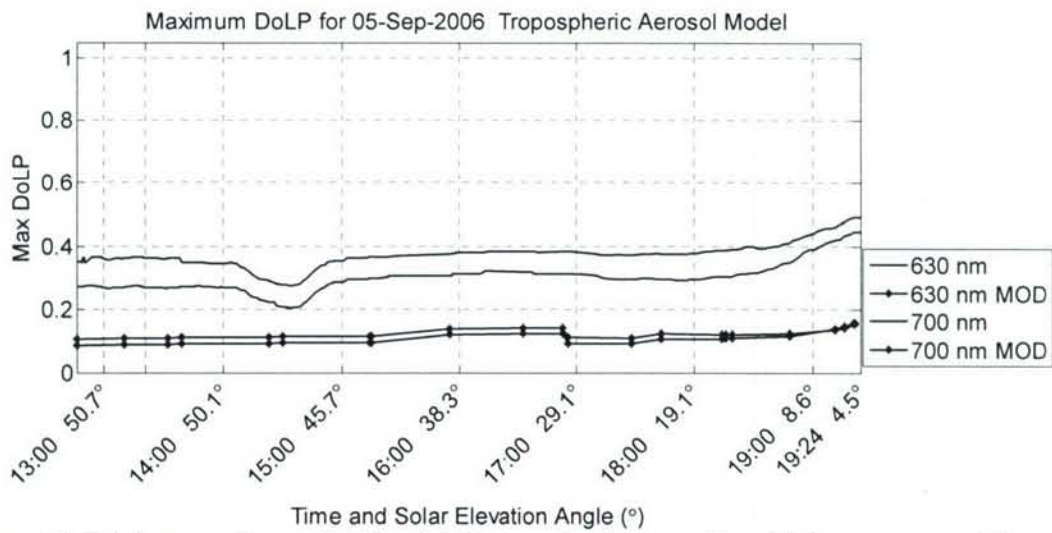
Figure 57. High-aerosol max DoLP with Tropospheric aerosol multiple-scatter model 630, 700 nm.
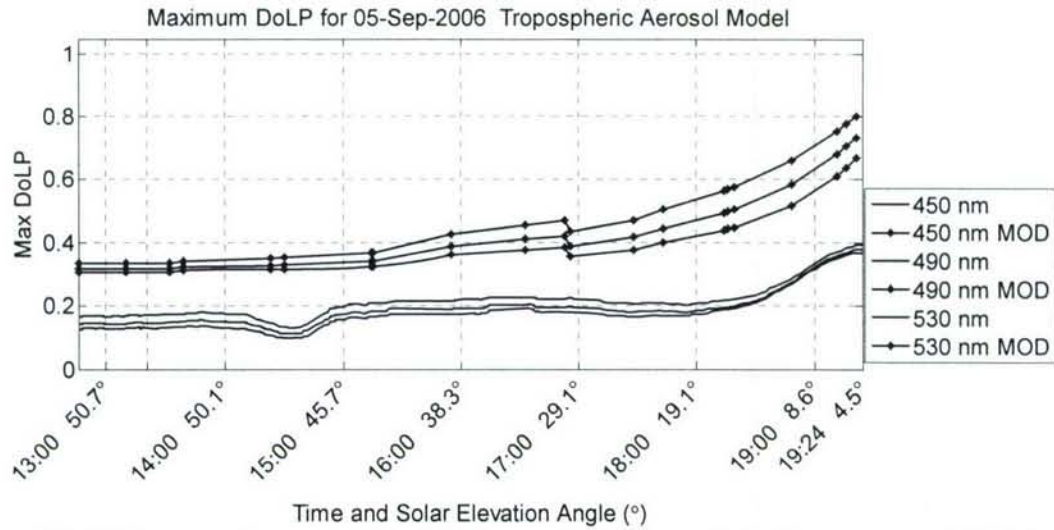
**Figure 58.** High-aerosol max DoLP with Tropospheric aerosol single-scatter model 450-530 nm.
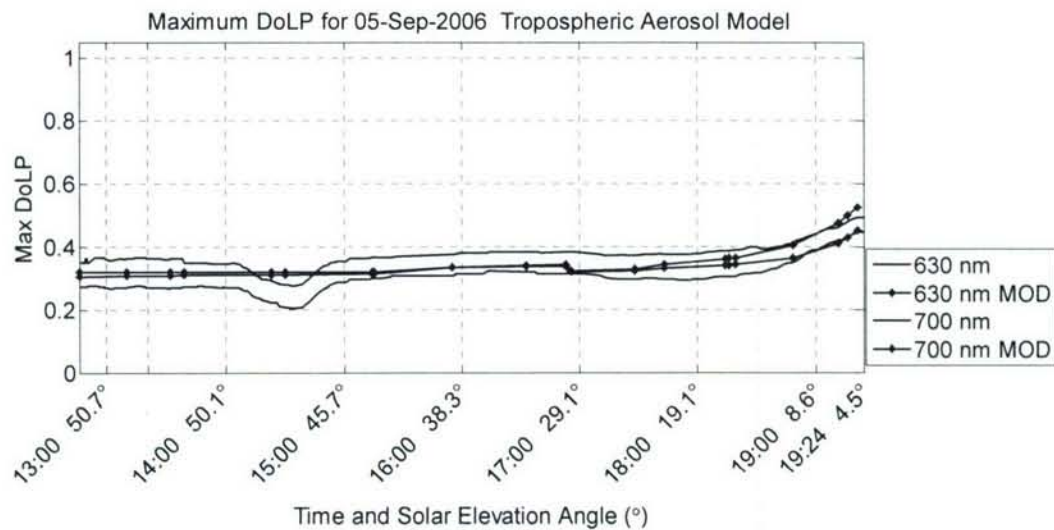
Figure 59. High-aerosol max DoLP with Tropospheric aerosol single-scatter model 630, 700 nm.

Zenith Slice Comparisons with MODTRAN-P

Although the maximum degree of polarization is the primary variable to be validated in the clear sky model, it was also desired to compare the model with measurement s made in sky regions away from the maximum degree of polarization. Since the mid-day September 25, 2006 clear-sky data seemed to be accurately modeled for 630 and 700 nm with a single-scatter model using the Rural aerosol type, these cases were used to assess the DoLP accuracy through a slice of the sky that included the solar position and zenith. The time of both slices was picked to be 13:00. Figures 60 and 61 show the results for both scattering models at 700 nm.
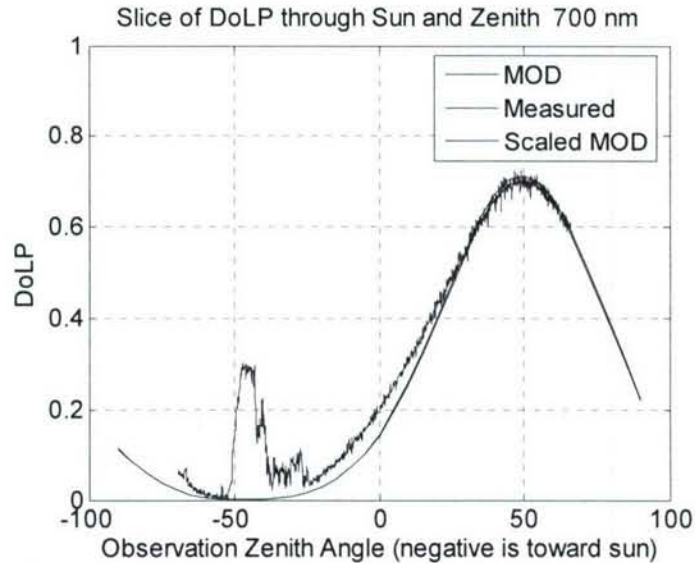
Figure 60. DoLP image slice at 13:00 MDT on September 25, 2006 with single-scatter model 700 nm. The green line shows the results of the model if it were to be scaled to have identical maximum DoLPs as the data. The bump in the measured data near the model zero is caused by the sun occulter. (This is the reflected DoLP of the back of the sun occulter.)
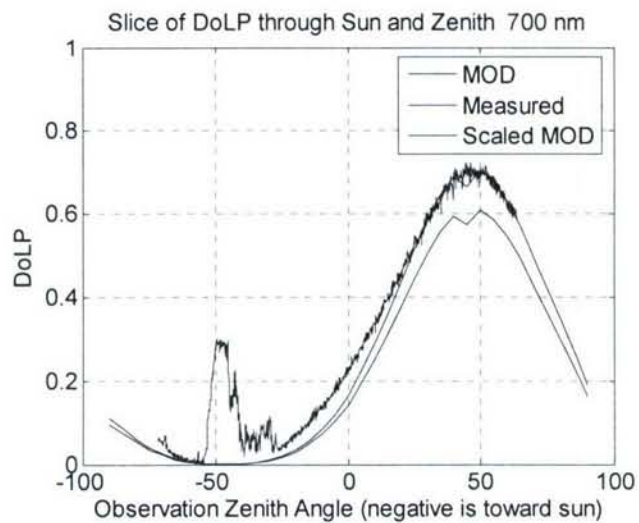
Figure 61. DoLP slice at 13:00 MDT on September 25, 2006 with multiple-scatter model 700 nm. The green line shows the results of the model if it were to be scaled to have identical maximum DoLPs as the data. The bump in the measured data near the model zero is caused by the sun occulter. (This is the reflected DoLP from the back of the sun occulter.) The bump in the model near the maximum appears to be a problem with the MODTRAN model itself, not input parameters.

Since the exact observation zenith angle for each pixel in the image is not known, the plot of the actual data was obtained by the following procedure: First, the angle of

polarization image was displayed. Using the contour lines of the angle of polarization, the confluence of these lines (which happens at each neutral point) was used to approximate the exact position of the sun behind the solar occulter. The center of the image was estimated and the DoLP was extracted from a line that included these two points. The spike in the DoLP (red line) is not actual sky data, but displays the DoLP of the underside of the occulter. Visual fitting of the data confirms that the minimum DoLP of the model aligns with the solar position estimate. Second, the maximum DoLP was found for both the model and the actual data. Third, the data slice was stretched linearly to align the minimum of the data to the estimated solar point and the maximum of the data to the maximum of the model. This linear stretching is valid only if the 16-mm fisheye lens actually uses a true equidistance projection—which Nikon claims it does. Finally, to allow comparison of the model to the actual data, the entire model was scaled to match the model maximum DoLP with the actual maximum DoLP (green line).

Inspection of the plots proves that near the point of maximum DoLP, the model accurately predicts the DoLP. Near the sun, neither model predicts the two neutral points, but instead shows one neutral point at the solar point. This is due to the invalid treatment of multiple scattering. In spite of the uncertainties in the exact location of the sun under the occulter, it can be confidently concluded that between 25° and 50° from the sun the DoLP is under-predicted by both models. (This is the area of the plot around 0° of observation zenith angle.) This conclusion is also supported by the 630-nm slice, which shows similar characteristics (Figures 62 and 63).
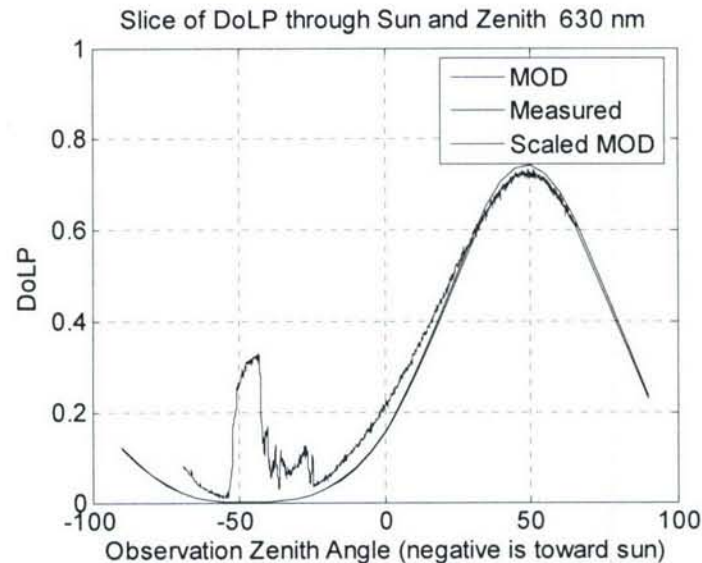
Figure 62. DoLP Slice at 13:00 MDT on September 25, 2006 for 630 nm with Single-scatter Model. The bump in the measured data near the model zero is the sun occulter. (This is the reflected DoLP from the back of the sun occulter.)
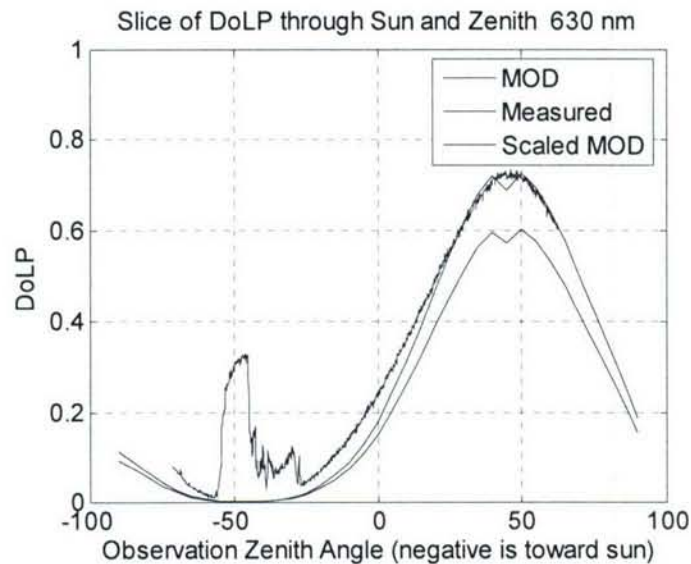
Figure 63. DoLP Slice at 13:00 MDT on September 25, 2006 for 630 nm with Multiple-scatter Model. The green line shows the results of the model if it were to be scaled to have identical maximum DoLPs as the data. The bump in the measured data near the model zero is the sun occulter.

For both wavelengths, the single-scatter model is a slightly better model with maximum errors being about 5%, while the multiple-scatter model had errors as much as 6%. Close inspection of the plots reveals that the observed zenith angle of maximum degree of polarization for the multiple-scatter models is about 2° closer to the sun than the single-scatter models. Since this is a significant difference, absolute calibration of the angle of observation for the instrument should be considered for future MODTRAN-P validation work.

Summary and Conclusions

A dual-field (telephoto and full-sky) imaging polarimeter has been designed for measuring the effect of varying sky polarization on the polarization signatures of ground-based objects and for validating polarized radiative transfer codes. This system employs liquid crystal variable retarders (LCVRs) to rapidly vary the polarization state of the measurements to minimize errors caused by changing sky conditions. Calibrating each pixel at every wavelength and f/# allows for compensation of the incidence-angle dependence of LCVR retardance. The system is being used to study sky polarization as a function of variable cloudiness. Initial data show good agreement with previous measurements for clear skies and show that clouds can alter the polarization of light in clear parts of a partly cloudy sky.

Specific conclusions from this study are summarized below.

1. The dual-LCVR approach provided adequate speed and accuracy for a full-sky imaging polarimeter. This is the first system that has been reported in the open

literature with the capability of measuring full-sky polarization with changing clouds and provide polarimetrically calibrated digital output data.

2. The degree of linear polarization (DoLP) in the atmosphere increases with wavelength in a clear sky. However, the DoLP decreases with wavelength in the clear portion of a partly cloudy sky.

3. The DoLP in a clear portion of a partly cloudy sky is consistently much less than that in a fully clear sky. We believe that this is caused by cloud droplets that have not quite formed a visible cloud, but it is very difficult to either determine or describe the difference between subvisual cloud droplets and aerosols. Further studies will require a steerable, calibrated aerosol lidar.

4. Clouds generally appear unpolarized, or with very low DoLP, but polarized skylight below a cloud is often detectable with an upward-viewing polarimeter. The observed DoLP depends on the optical properties in the path, and on the radiometric contrast between the path-scattered light and the cloud-scattered light.

5. The DoLP observed in Bozeman, Montana with very low aerosol content approaches the values reported in the literature for measurements taken at the pristine Mauna Loa, Hawaii facility. Future measurements are being planned with our polarimeter at Mauna Loa to provide measurements that can be compared with a pure Rayleigh atmosphere model.

6. The Angle of Polarization has been observed to be altered in the presence of some clouds. Further studies will be required to understand this more completely, but this is an important result that is in conflict with some previously published statements.

7. A 22-degree halo has been observed with this imaging polarimeter. The results provide valuable experimental confirmation of previously published theories.

MODTRAN-P Validation

8. Multiple-scatter models—with one exception—consistently under-predict the DoLP for all wavelengths because of the inappropriate modeling of the multiple scattered component as completely unpolarized. For low-aerosol skies, these models preserve the shape of the maximum DoLP near sunrise and sunset, but for larger optical depths they begin to lose their shape. Single-scatter models perform exactly opposite. They are too flat for low-aerosol skies, but for high optical depths they match the shape of the sunset/sunrise data almost exactly.

9. For all wavelengths above 600 nm, the multiple-scatter and single-scatter models can be used as a bound on the DoLP. The multiple-scatter model is lower than the measured data, while the single-scatter model is always higher than measured data.

10. For a low-aerosol sky, single-scatter models are accurate to within instrument accuracy during the mid-day for wavelengths greater than 600 nm when either the Urban aerosol type or the Rural aerosol type is used. As the total optical depth at 500 nm increases above 0.20, the accuracy of the model moves above the error bounds of the instrument. For shorter wavelengths, the single-scatter model consistently over-predicts the maximum DoLP. This is expected because the wavelength dependence of Rayleigh scattering causes multiple scattering to be larger at shorter wavelengths.

11. For solar elevations near sunrise and sunset, single scatter models are less than adequate for the long wavelengths. The models consistently under-predict the DoLP in these regions. This suggests that the dependence of the DoLP reduction on aerosol extinction may be too extreme. The model seems to be too sensitive to total extinction in the boundary layer.

12. The standard Tropospheric aerosol type performs worse than the Urban and Rural types for all multiple-scatter models. Conversely, when used in the single-scatter model, the Tropospheric aerosol type performs the best overall for the three days. For mid-day data, maximum errors of 10% could be expected for 630 and 700 nm. Since multiple scattering is not a driving variable at these wavelengths, this suggests that the aerosol content from the forest fires most closely matched this standard aerosol model in the long wavelengths.

13. Aerosol type is a highly important variable. For high-aerosol-content skies, the difference between the models can be as much as 20%. For low aerosol content skies, the difference between models can be as much as 10%. For some special cases, these problems are not severe. For example, any of the standard aerosol models predict a fairly accurate polarization above 600 nm when used with the single-scatter model. Nevertheless, a complete MODTRAN-P validation will need instrumentation and software that can generate aerosol phase functions from an aerosol size distribution and complex refractive index. (MODTRAN-P also needs to be updated to handle this information.)

14. Modeling of the zenith slice through the sun showed than the DoLP in the region of the sun and the region of maximum degree of polarization was accurate. Still, the neutral points are not seen in the model because of the improper implementation of multiple scattering. Also, model regions that were 25° to 50° from the sun exhibited DoLPs of about 5% less than the measurements.

References

Bohren, C. 1996. Atmospheric optics. In *Encyclopedia of Applied Physics*, 53-91. New York: VCH Publishers.

Cattrall, C.; Reagan, J.A.; Thome, K.; Dubovik, O. 2005. Variability of aerosol and spectral lidar and backscatter and extinction ratios of key aerosol types derived from selected Aerosol Robotic Network locations. JOURNAL OF GEOPHYSICAL RESEARCH 110: D10S11.

Chipman, R. 2005. Depolarization index and the average degree of polarization. APPLIED OPTICS 44: 2490-2495.

Conant, J.; Iannarilli, F.; Bacon, F.; Robertson, D.; Bowers, D. 2005. PPACS – a system to provide measured atmospheric aerosol/molecular conditions to EO/IR simulations. Aerodyne Research, Inc. (accessed Nov. 28, 2006). http://www.aerodyne.com/cosr/PPACSWebPages/Conant_PPACS_AtTrPaper_v4.pdf

Coulson, K. 1988. *Polarization and intensity of light in the atmosphere*. Hampton: Deepak Publishing.

Fetrow, M. 2006. Air Force Research Laboratory, Albuquerque, NM. Personal Correspondence.

Horvath, G; Barta, A; Gal, J; Suhai, B; Haiman, O. 2002. Ground-based full-sky imaging polarimetry of rapidly changing skies and its use for polarimetric cloud detection. APPLIED OPTICS 41 (3): 543-559.

Kattawar, G; Plass, G. 1972. Degree and direction of polarization of multiple scattered light. 1: Homogenous Cloud Layers. APPLIED OPTICS 11 (12): 2851-2865.

Können, G.P.; Wessels, H; Tinbergen J. 2003. Halo polarization profiles and sampled ice crystals: observations and interpretation. APPLIED OPTICS 42 (3): 309-317.

Können, G.P.; Muller, S; Tinbergen J. 1994. Halo polarization profiles and the interfacial angles of ice crystals. APPLIED OPTICS 33 (21): 4569-4580.

Können, G.P.; Tinbergen, J. 1991. Polarimetry of a 22° halo. APPLIED OPTICS 30 (24): 3382-3400.

Können, G.P. 1983. Polarization and intensity distributions of refraction halos. JOURNAL OF OPTICAL SOCIETY OF AMERICA 73 (12): 1629-1640.

Kovalev V.A.; Eichinger, W.E. 2004. *Elastic lidar*. New York: Wiley-Interscience.

Liu, Y; Voss, K. 1997. Polarized radiance distribution measurement of skylight 2. Experiment and data. APPLIED OPTICS 36 (33): 8753-8764.

Lynch, D. 1979. Polarization models of halo phenomena I. The parhelic circle. JOURNAL OF THE OPTICAL SOCIETY OF AMERICA 69 (8): 1100-1103.

North, J.A.; Duggin, M.J. 1997. Stokes vector imaging of the polarized sky-dome. APPLIED OPTICS 36 (3): 723-730.

Pust, N. J., 2007. *Full sky imaging polarimetry for initial polarized MODTRAN validation,* Ph.D. Dissertation, Montana State University, Bozeman, Montana.

Pust, N.J.; Shaw, J.A. 2006. Dual-field imaging polarimeter using liquid crystal variable retarders. APPLIED OPTICS 45 (22): 5470-5478.

Sabatke, D. S., M. R. Descour, E. L. Dereniak, "Optimization of retardance for a complete Stokes polarimeter," Optics Letters **25**, 802-804 (2000).

Schuster, G.L. 2006. Angstrom exponent and bimodal aerosol size distributions. JOURNAL OF GEOPHYSICAL RESEARCH 111 (d7): D07207.

Seldomridge, N. 2005. Dual polarization cloud LIDAR design and characterization. Master's thesis, Montana State University. Online. Available: http://etd.lib.montana.edu/etd/view/item.php?id=68

Seldomridge, N.L.; Shaw, J.A.; Repasky K.S. 2006. Dual-polarization lidar using a liquid crystal variable retarder. Optical Engineering 45(10): 106202.

Shaw, G.E. 1983. Sun photometry. BULLETIN OF THE AMERICAN. METEOROLOGICAL. SOCIETY. 64(1): 4-10.

Spinhirne, J. D.; Reagan, J.A; Herman B.M. 1976. Vertical distribution of aerosol extinction cross section and inference of aerosol imaginary index in the troposphere by lidar technique. JOURNAL OF APPLIED METEOROLOGY 19: 426-438.

Tyo, J.S. 2000. Noise equalization in Stokes parameter images obtained by use of variable-retardance polarimeters. OPTICS LETTERS 25 (16): 1198-1200.

Tyo, J.S. 2002. Design of optimal polarimeters: maximum of signal-to-noise ratio and minimization of systematic error. APPLIED OPTICS 41 (4): 619-630.

Tyo, J.S., D. Goldstein, D. Chenault, J. A. Shaw, 2006. Review of passive imaging polarimetry for remote sensing applications. APPLIED OPTICS 45(22): 5453-5469.

Voss, K.J.; Liu, Y. 1997. Polarized radiance distribution measurements of skylight .1. System description and characterization. APPLIED OPTICS 36 (24): 6083-6094.

Xiao, X.; Voelz, D.; Sugiura, H. 2003. Field of view characteristics of a liquid crystal variable retarder. PROCEEDINGS OF THE SPIE VOL. 5158: 142-150.

Publications Produced with Full or Partial Support from this Grant

Journal Papers

Seldomridge, N. L. J. A. Shaw, and K. S. Repasky (2006). "Dual-polarization lidar using a liquid crystal variable retarder," *Optical Engineering* **45**(10): 106202.

Pust, N. J. and J. A. Shaw (2006). "Dual-field imaging polarimeter using liquid crystal variable retarders," *Applied Optics* **45**(22): 5470-5478.

Tyo, J. S., D. L. Goldstein, D. B. Chenault, and J. A. Shaw, (2006). "A Review of passive imaging polarimetry for remote sensing applications," *Appl. Opt.* **45**(22), 5453-5469.

Tyo, J. S., D. L. Goldstein, D. B. Chenault, and J. A. Shaw, (2006). "Polarization in Remote Sensing - Introduction," Special issue on Polarization Imaging in Remote Sensing, *Appl. Opt.* **45**(22), 5451-5452.

B. Thurairajah and J. A. Shaw (2005). "Cloud statistics measured with the Infrared Cloud Imager," *IEEE Trans. Geosci. Rem. Sens.* **43**(9), 2000–2007.

J. A. Shaw, P. W. Nugent, N. J. Pust, B. Thurairajah, and K. Mizutani (2005). "Radiometric cloud imaging with an uncooled microbolometer thermal infrared camera," *Opt. Express* **13**(15), 5807–5817.

Conference Papers

J. A. Shaw, "A review of thermal infrared polarization in the outdoors," Invited Talk, *Infrared Detectors and Focal Plane Arrays* (SPIE), San Diego, CA, Aug. 2007.

P. W. Nugent, J. A. Shaw, M. Kehoe, C. Smith, T. Moon, and R. Swanson, "Measuring the MTF of imaging spectrometers at infinite focus with roof-line images," *Imaging Spectrometry XII* (SPIE), San Diego, CA, Aug. 2007.

P. W. Nugent, J. A. Shaw, and S. Piazzolla, "Wide-angle infrared cloud imaging for measuring cloud statistics in support of Earth-Space optical communication," in *Free-Space Laser Communications VII* (SPIE), San Diego, CA, Aug. 2007.

N. J. Pust and J. A. Shaw, "All-sky imaging polarimetry," in *Polarization Scence and Remote Sensing III* (SPIE), San Diego, CA, Aug. 2007.

J. A. Shaw, N. L. Seldomridge, and K. S. Repasky, "Polarization lidar using a liquid-crystal variable retarder," 23rd International Laser Radar Conference (ILRC), Nara, Japan, 24-28 July 2006.

N. J. Pust and J. A. Shaw, "Dual-field polarization imager development and calibration," Optical Technology Center (OpTeC) annual meeting, Montana State University, Bozeman, MT, 22–23 Sept., 2005.

N. J. Pust and J. A. Shaw, "Imaging spectro-polarimetry of clear, cloudy, and smoke-filled skies," Optical Technology Center (OpTeC) annual meeting, Montana State University, Bozeman, MT, 18–19 Sept., 2006.

N. Seldomridge, J. A. Shaw, and K. S. Repasky, "Dual-polarization cloud lidar using a liquid crystal variable retarder," *SPIE Proceedings* **5888** (Polarization Science and Remote Sensing II, J. A. Shaw and S. Tyo, Eds.), San Diego, CA, 2–4 Aug., 2005.

N. J. Pust and J. A. Shaw, "Dual field imaging polarimeter for studying the effect of clouds on sky and target polarization," *SPIE Proceedings* **5888** (Polarization Science and Remote Sensing II, J. A. Shaw and S. Tyo, Eds.), San Diego, CA, 2–4 Aug., 2005.

Theses

Seldomridge, N. L. (2005). "Dual polarization cloud LIDAR design and characterization," Master of Science thesis, Montana State University. Available online: http://etd.lib.montana.edu/etd/view/item.php?id=68

Pust, N. J. (2007). "Full sky imaging polarimetry for initial polarized MODTRAN validation," Ph.D. Dissertation, Montana State University, Bozeman, Montana. Available online: http://etd.lib.montana.edu/etd/view/item.php?id=489